

A Comprehensive Characterization of the Vacuum Beam Guide and Its Applications

Yuxun Huang,^{1,*} Delaney Smith,¹ Pei Zeng,¹ Debayan Bandyopadhyay,¹ Junyu Liu,² Rana X Adhikari,^{3,†} and Liang Jiang^{1,‡}

¹*Pritzker School of Molecular Engineering, The University of Chicago, Chicago, IL 60637, USA*

²*Department of Computer Science, The University of Pittsburgh, Pittsburgh, PA 15260, USA*

³*Division of Physics, Math, and Astronomy, LIGO Laboratory, California Institute of Technology, Pasadena, CA 91125 USA*

(Dated: January 27, 2026)

The proposed vacuum beam guide (VBG) represents a transformative advance in quantum channel technology, guaranteeing an ultra-low level of attenuation and a broad transmission linewidth, which offers an unprecedented quantum capacity, exceeding Tera-qubits per second on a continental scale. However, the stability of the VBG in terms of interferometry remains unexamined. To address this gap, we have developed a comprehensive noise budget for sources of phase noise in the VBG, highlighting its capabilities for precision interferometry. This model facilitates a comprehensive characterization of the VBG as a photonic quantum channel, thereby allowing a detailed investigation of its potential. Our theoretical analysis finds no technical or fundamental blockers for a VBG and predicts its expected performance in a wide range of quantum applications.

I. INTRODUCTION

Creating a low-loss quantum channel for global networks is challenging due to optical absorption losses that cause an exponential drop in direct quantum communication rates with distance, thereby restricting the function of fiber and free-space channels to tens of kilometers [1–4]. While improvements in quantum communication range have been made, current satellite-based channels are costly, fragile, and weather-dependent [5–8]. Meanwhile, the quantum repeaters currently available still lack full error correction ability, and their use results in a polynomial reduction in communication rates across long distances [9].

An entirely distinct approach to counteracting the attenuation encountered in optical channels is provided by the vacuum beam guide (VBG) [10]. This system holds substantial promise for establishing the fundamental framework of a global-scale quantum network due to its inherent resilience and practicality, all of which can be achieved using current technology. Optical channel specifications typically highlight key metrics, including attenuation, transmission linewidth, interference stability, polarization, transmission delay, and dispersion. The first three are crucial for defining the noise model of the quantum channel and thus the quantum capacity across various coding schemes [11–15], while other metrics may serve specific needs. By conceptualizing the VBG as a pure-loss channel [11, 14], the quantum channel capacity is projected to exceed Tera-qubits per second, which is asymptotically achievable with the appropriate implementation of phase-insensitive dual-rail encoding [16]. Nevertheless, certain scenarios pose chal-

lenges in performing or modifying such encodings, particularly within the domain of quantum metrology, where information is intrinsically encoded by nature. For applications such as long-baseline optical telescopes, achieving interferometric stability is crucial to suppress dephasing that would otherwise destroy any prospective quantum coherence [17, 18].

A comprehensive description of the VBG as a bosonic channel is essential, as it lays the groundwork for investigating potential applications and allows for the relaxation of constraints on encoding schemes. The stability of the VBG as a set of interferometers can be evaluated using the phase noise power spectral density (PSD), denoted $S_\phi(f)$ [19, 20]. This PSD is composed of dozens of noise sources, including both fundamental and technical aspects. Typically, the PSD associated with a particular noise source is derived from small-scale characterization experiments and/or detailed models. The noise sources are separated in this way for ease of analysis. In most cases, it is assumed that the noise from each source is random and statistically uncorrelated with any others. Leveraging early theoretical insights from LIGO and practical performance data from the O1-O4 observational runs [21–23], we have developed a comprehensive phase noise model for the VBG. Given LIGO’s stringent stability demands for gravitational wave detection [24], it may be unsurprising that the estimated performance of the VBG illustrates notable advantages beyond 10 Hz over the limit set by the fiber thermal noise floor, but we show that the VBG is capable of accomplishing this using a considerably simpler control system than LIGO, as detailed in Appendix. A.

This noise analysis enables us to identify direct applications that span the categories of secure quantum communication, distributed quantum sensing, and federated quantum computing. Our numerical investigations reveal a significant scaling enhancement, which clearly illustrates the versatile nature and substantial advantages conferred by the VBG.

* yesunhuang@uchicago.edu

† rana@caltech.edu

‡ liangjiang@uchicago.edu

II. CHARACTERIZATION OF THE VBG

The VBG utilizes an array of precisely aligned lenses and mirrors within a long vacuum tube to guide the photons that carry the quantum information. A sketch of the VBG is shown in Fig. 1(a). The VBG is composed of N_{tot} sections, each of length L_0 , and lenses with a diameter of $2R$ to guide the light signal over a distance of $L_{\text{tot}} = N_{\text{tot}}L_0$. In order to traverse a continent, the light path will need to bend to avoid existing structures and save on construction costs. Flat steering mirrors will be mounted inside the tube to make these static deflections, as well as to provide active steering. To ensure low absorption and perturbation from the air, the entire beam path must be in a vacuum, albeit at a modest pressure ($\lesssim 1$ Pa at room temperature). The baseline design is summarized in Table. I [10]. This configuration serves as the foundation for estimating the performance metrics, the values of which, together with the relevant applications, are summarized in Fig. 3.

TABLE I. Baseline Parameters of the VBG

Parameters	Symbol	Values
Section Length	L_0	4 km
Focus Length	f	2 km
Lens Radius	R	12 cm
Center Wavelength	λ_c	1550 nm
Spot Size	w	4 cm
Operating Pressure	P	1 Pa
Operating Temperature	T	~ 300 K

A. Attenuation

As the beam travels mostly in a vacuum in the VBG, it is an ultra-transparent channel with extremely low loss ($\sim 10^{-5}$ dB/km). In addition, in contrast to satellite-to-ground links, a buried VBG is ground-based, stable, robust against environmental disturbances, and can be operated at all times. Most importantly, the VBG does not suffer from the baseline 3 dB loss introduced by the thickness of the atmosphere, which is almost inevitable for satellite-to-ground links [5]. The total effective attenuation of the VBG, $\alpha_{\text{tot}}(\lambda)$, in the normalized unit of dB/km, can be divided into the following four main contributions,

$$\alpha_{\text{tot}}(\lambda) = \alpha_{\text{lens}} + \alpha_{\text{gas}} + \alpha_{\text{align}} + \frac{L_0}{L_{\text{mirror}}} \alpha_{\text{mirror}}, \quad (1)$$

where α_{lens} denotes the total loss of the lens due to absorption, scattering, diffraction, and reflection from the anti-reflection (AR) coatings; α_{gas} is the loss of the residual gas, dominated by absorption; α_{align} is due to the imperfect alignment of the lenses, which leads to the leakage of energy into higher-order transverse modes. The first three terms constitute the baseline loss of the VBG chan-

nels, as estimated in the previous analysis [10]. The angular alignment of the steering mirrors is crucial and may impose additional loss, which is captured in the last term and analyzed in detail in Appendix. A 2, where L_{mirror} denotes the distance between two neighboring steering mirrors.

The attenuation spectrum of the VBG around the telecom band, assuming the baseline configuration, is numerically calculated and plotted in Fig. 1(b). Compared with the state-of-the-art fiber and satellite-to-ground channels, the VBG low-loss passband centered at $\lambda_c \approx 1550$ nm offers at least a two-order-of-magnitude reduction in attenuation. The loss due to the steering mirrors is estimated in Appendix and repeated here for convenience:

$$\bar{\alpha}_{\text{VBG}} \approx 4 \times 10^{-5} \text{ dB/km}; \quad (2)$$

$$\bar{\alpha}_{\text{VBG(SMirrors)}} \approx 5 \times 10^{-5} \text{ dB/km},$$

$$\Delta \bar{\alpha}_{\text{VBG(SMirrors)}} \approx 10^{-5} \text{ dB/km}. \quad (3)$$

B. Linewidth

In addition to the ultra-low attenuation achieved at the center frequency, the linewidth, or transmission window, is crucial for time-, frequency-, or hybrid-division multiplexing and thus directly contributes to the total quantum capacity. The VBG attenuation spectrum allows for a broad linewidth of roughly $\Delta\lambda = 50$ nm or $\Delta\nu \approx \frac{c\Delta\lambda}{\lambda_c^2} = 6$ THz, across which the VBG maintains its attenuation factor. The transmission efficiency at a given wavelength λ can be determined using the attenuation factor as $\eta(\lambda) = 10^{-0.1L_{\text{tot}}\alpha(\lambda)}$. Following this, the pure-loss capacity per channel use is defined as [11, 12, 25]:

$$q_k(\lambda) = \max \left[\log_2 \left(\frac{\eta^{2-k}(\lambda)}{1 - \eta(\lambda)} \right), 0 \right], \quad (4)$$

where $k = 1, 2$ corresponds to one- or two-way quantum communication. Notably, the one-way model is shown to be constructively realizable with appropriate encoding [26, 27].

The maximum transmission rate of quantum information through multiplexing in quantum communication protocols can be obtained (in units of qubits per second) by integrating q_k [13]:

$$Q_k \equiv \int q_k d\nu = \int q_k(\lambda) \frac{c}{\lambda^2} d\lambda. \quad (5)$$

The wide transmission window of the VBG enables it to achieve a remarkable capacity of Tera-qubits per second over a continental distance (10^4 km), as shown in Fig. 1 (c). Quantitative evaluation of the VBG's channel capacity shows substantial superiority compared to state-of-the-art systems [5, 10].

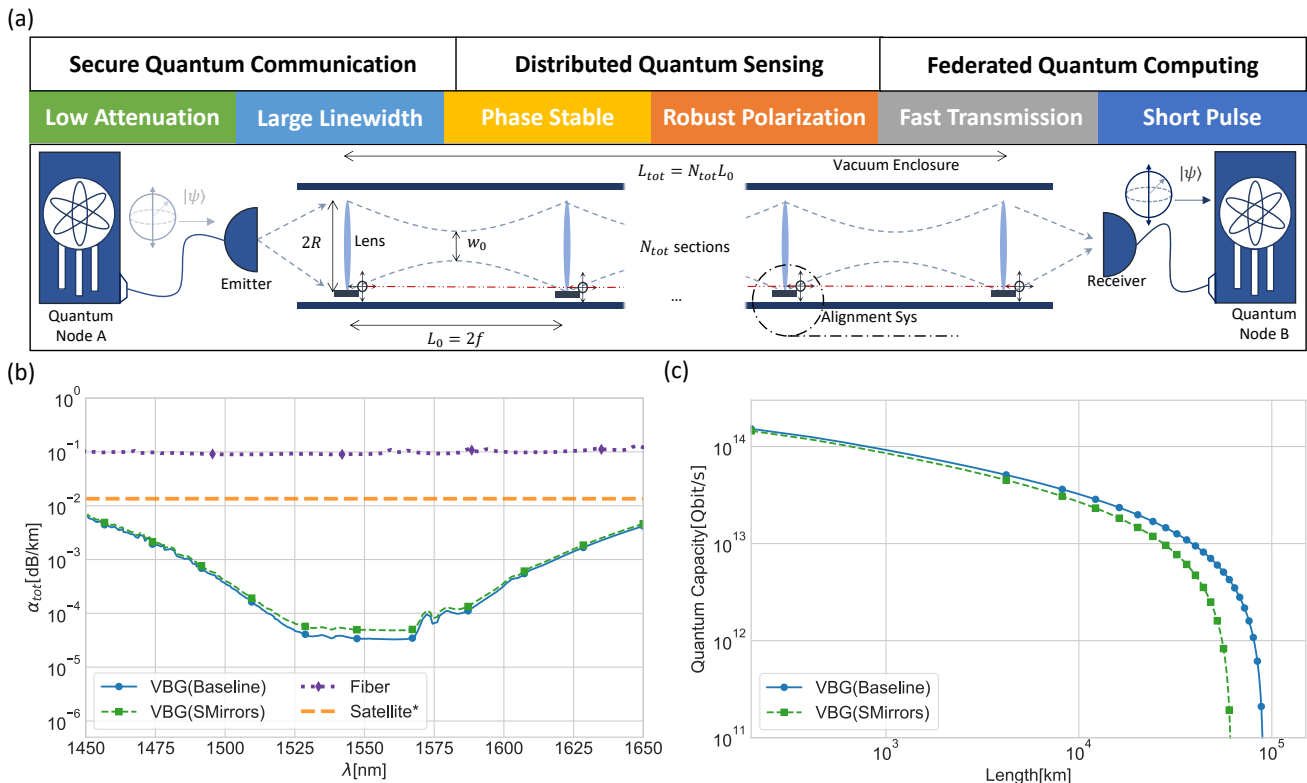


FIG. 1. The illustration and performance of the VBG and additional loss from flat mirrors at room temperature and a residual gas pressure of $P = 1$ Pa. The relative alignment accuracy of each lens and mirror is assumed to be 0.1% for vertical translation and 1% for parallel translation w.r.t the optical axis. (a) Schematic diagram of the VBG along with a representative collection of capabilities and applications. (b) The attenuation factor of the VBG compared to the SOTA fiber (Experimental data presented here while theoretical limit is greater than 0.01 dB assuming practical constrains) [1, 2] and the satellite-to-ground link (*approximate level) [5, 7]. (c) The quantum capacity of VBG under one-way protocols (Two-way protocols show similar results).

C. Phase Noise Power Spectral Density

Phase noise is sometimes regarded as less important than attenuation loss because straightforward coding strategies, such as time-bin or polarization encoding, can mitigate it. Phase noise, however, does pose a constraint when using a VBG as the foundation for global-scale quantum networks. Input/output channels linked to the VBG might implement particular coding methods, such as GKP codes [16, 27–29], to counteract loss. Some of these methods are less robust against phase noise, necessitating a coding conversion that would diminish quantum fidelity. Numerous QKD protocols also use single rail encoding to improve communication distance and security [30–33], where fluctuations in the optical path length scramble the relative phase between the vacuum and single-photon components, resulting in direct dephasing of the qubit. More critically, in many quantum sensing schemes, the encoding is intrinsic to the sensing entity and is sensitive to both attenuation and phase noise [34, 35]. Converting between coding schemes can compromise quantum advantages or restrict parameter

ranges. Therefore, it is essential to carefully analyze and mitigate all important sources of phase in the VBG channel to maintain its versatility.

Noise sources corresponding to a particular application scheme can be broadly classified into two main categories: channel-added noises and those associated with source-detection processes. The former refers to the intrinsic noise attributed to the VBG channel itself, while the latter stems from the quantum sources and the details of detection methodologies, including examples such as vibrations in the injection and detection optics, noise in the photodetectors, fluctuations in the laser source’s amplitude/frequency, and shot noise, which are not directly related to the channel characteristics. This section is dedicated to estimating only the channel-added noise, as the noise associated with quantum sources and detection methods is determined by the specific application scheme.

Unlike attenuation noise, the total phase noise for certain applications is not always the overall RMS noise but is rather determined by the frequency band of the signal of interest. The noise outside of the band can usually be filtered out optically, electronically, or numerically. We

will characterize each noise source in terms of its phase noise power spectral density (PNPSD), $S_\phi(f)$. In addition, we normalize the amplitude spectral density (ASD, square root of the PSD) with the total distance to obtain $\sqrt{\hat{S}_\phi}$ in the unit of $(\text{rad}/\sqrt{\text{Hz} \cdot \text{km}})$, assuming that the noises from each VBG section are random and uncorrelated. In Appendix. A, we describe the prototype design of the VBG control system, which consists of the Passive Isolation Platform (PIP), the Alignment Sensing System (ACS), and the Section Length Stabilization (SLS) system used to stabilize the alignment and vibrations of each section.

The overall phase noise amplitude spectral density of the VBG under the baseline configuration is shown in Fig. 2 (a) and is compared to the fundamental thermal noise of fibers. The detailed noise budget is included in Appendix. B. The ASD scales roughly as $\frac{1}{f^3}$ in the 1–100 Hz band and $\frac{1}{f^2}$ beyond, limited by seismic noise (filtered by PIP). The mount thermal noise and the residual gas scattering cause a bump around 0.1 and 10 kHz, respectively, followed by a flattening at high frequencies introduced by mirror thermal noise. Noise below 10 Hz can be suppressed by the active SLS system with the heterodyne round-trip phase noise cancellation technique [36], at the cost of degraded high frequency performance due to the limitations of sensing noise and closed-loop causality. The integration of $S_\phi(f)$ over the specified signal band gives rise to the dephasing factor γ in the common quantum information literature [15]. The cumulative noise (integrated up to 10^6 Hz) under various lower cutoff frequencies f_l is also plotted in Fig. 2 (b). The integrated RMS phase noise per square-root kilometer of the VBG, before and after active subtraction, is at the level of 0.3 rad and 1 mrad, respectively, which is capable of outperforming fiber when the lower cutoff frequency $f_l > 10$ Hz. The phase stability of the VBG can certainly be improved using LIGO-like technology [37, 38]. The majority of the improvement would come from using active vibration isolation platforms for all of the lenses and mirrors [39, 40], although this would be enormously expensive.

D. Polarization, Transmission Speed and Pulse Duration

In addition to the three critical metrics introduced above, we also briefly discuss the performance of the VBG in polarization maintenance, transmission speed, and the pulse duration limit.

Polarization maintenance is important for a general photonic quantum channel, as it is widely adopted in both satellite and fiber techniques. In polarization-based dual-rail encoding, the degradation of fidelity arises from both amplitude and phase, which are coupled together and cannot be simply represented by attenuation or dephasing, as detailed in Appendix. B 4. The noise is

mainly attributed to the misalignment of the reference plane of each optical element, and the net effects of each section of the channel, in addition to the overall average attenuation, can be approximately described by the following two nontrivial Kraus operators,

$$\{K_\alpha\} = \sqrt{p} \left\{ \begin{pmatrix} 0 & 1 \\ -1 & 0 \end{pmatrix}, \begin{pmatrix} 0 & e^{i\bar{\phi}} \\ -e^{-i\bar{\phi}} & 0 \end{pmatrix} \right\}, \quad (6)$$

where $\bar{\phi} \sim 10^{-2}$ rad [44] is the average birefringence phase difference, and p can be computed by integrating over the relevant frequency range of the misalignment angle $\delta\theta$'s noise power spectrum as $p = 2 \int_{f_{\min}}^{f_{\max}} S_\theta(f) df$. One can also normalize the probability with $1/4$ km to obtain the effective dissipation coefficient, similar to the treatment in the previous section. The noise can also be suppressed with proper frequency filtering analysis. For a rough estimate of the worst-case effect, one can replace the integral with the rms value of $\delta\theta_{\text{rms}} \sim 10^{-3}$ rad [45] per section, which gives rise to a probability of 1 ppm and suggests that the polarization noise by the VBG is two orders of magnitude smaller than the attenuation under the default configuration. This result demonstrates the robustness of the VBG in transmitting polarization-encoded qubits.

Transmission speed of the non-monochromatic signal will be slowed down by the dispersion in the VBG channel and is calculated as the group velocity,

$$v_g = \frac{\partial \omega}{\partial k} = \frac{c}{n} \left(1 + \frac{\lambda}{n} \frac{\partial n}{\partial \lambda} \right) \equiv \frac{c}{n_g}. \quad (7)$$

Since most parts of the VBG are in a vacuum, the deviation from the speed of light in a vacuum shall come from the weighted average of the group velocity determined by the optical elements and the vacuum velocity as $\bar{v}_g = \frac{L_0}{\sum_i d_i / v_{g_i}}$, where $\{d_i\}$ denotes the sections with different group velocity indices n_g . For our VBG system, the deviation is dominated by the ultra-pure silica substrate, which has a thickness of roughly $d_{\text{substrate}} \approx 2$ cm for the worst-case consideration [46] and a group velocity index of $n_g \approx 1.46$ for the light centered at 1550 nm. Therefore, the average group velocity in the VBG is calculated as

$$\bar{v}_g \approx (1 - 7 \times 10^{-6})c, \quad (8)$$

which represents only a 10 ppm deviation and thus can be safely neglected under most circumstances.

Pulse duration will also be limited by the dispersion effects due to the spreading of the wave packet determined by the group-velocity dispersion (GVD) [47],

$$\text{GVD} \equiv \frac{\partial^2 k}{\partial \omega^2} = \frac{2}{c} \left(\frac{\partial n}{\partial \omega} \right) + \frac{\omega}{c} \left(\frac{\partial^2 n}{\partial \omega^2} \right). \quad (9)$$

As an unchirped beam with a Gaussian profile passing through relatively thick materials with a thickness of d_i , the expansion in pulse duration τ can be calculated as

$$\Delta\tau \approx \frac{2\text{GVD}^2 d_i^2}{\tau^3}, \quad |\Delta\tau| \ll \tau. \quad (10)$$

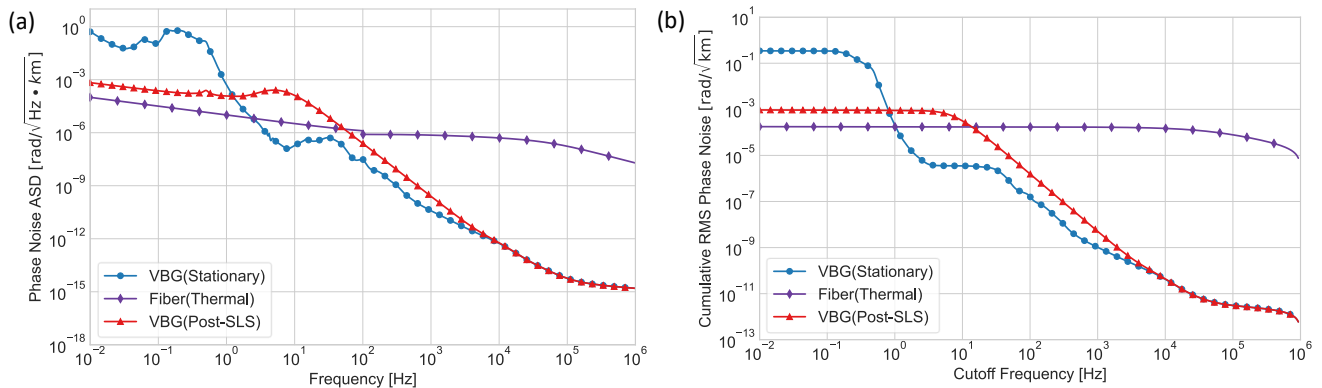


FIG. 2. Phase Noise Budget of the VBG assuming deployed in a relatively quiet, rural area (See Appendix. B). (a) Normalized phase noise ASD of the VBG before and after active cancellation in comparison with the fiber thermal noise floor [41–43]. (b) Cumulative phase noise.

The simulation shows that the group-velocity delay ($GDD \equiv GVD \times d_i$) of the coating is at least two orders of magnitude smaller than that of the substrate. Therefore, the expansion effects are dominated by the silica substrate with $GVD \approx -25.855 \text{fs}^2/\text{mm}$ at 1550 nm [48]. Suppose that the beam goes through $N \sim 10^4$ sections corresponding to a distance of 10^4km , and we require that the expansion of the duration is no larger than the original duration τ_{GVD} . Then, the duration of the pulse is lower bounded by

$$N\Delta\tau < \tau_{GVD} \Rightarrow \tau_{GVD} \gtrsim 50\text{fs}. \quad (11)$$

For comparison, the shortest pulse duration limited by the attenuation spectrum is given by

$$\tau_{\text{spectrum}} \geq \frac{1}{2\pi\Delta\nu} \sim 40\text{fs}, \quad (12)$$

which is close to the value limited by the dispersion.

III. NOTABLE APPLICATIONS

In Fig. 3, we summarize the applications of the VBG in three key areas. First, the capacity of the VBG for ultra-low-loss bosonic quantum state transmission enables it to surpass the theoretical QKD key rate limit of the current satellite-to-ground systems by four orders of magnitude and experimental results by eight orders under the basic QKD scheme [5, 10], suggesting its unique benefits for secure quantum communication. Moreover, the VBG’s high interference stability is crucial for overcoming significant hurdles in distributed quantum sensing, where naturally encoded signals typically experience phase noise that negates any quantum benefits [17, 18]. Finally, for federated quantum computing, particularly in cloud computing contexts [84–86], the VBG offers a key benefit of reducing transmission delays in addition to ensuring robust, high-bandwidth entanglement. To illustrate the claimed benefits in each key area, we highlight

a detailed quantitative analysis for implementing each of the following specific protocols: Device-Independent QKD (DI-QKD) [49, 54, 56], Quantum Telescope (Q-Telescope) [68–70], and Blind Quantum Computation (BQC) [79, 80]. For interested readers, a detailed illustration and performance estimation for the other mentioned protocols can also be found in the corresponding sections in Appendix, as shown in the caption of Fig. 3.

A. Device Independent QKD

DI-QKD is a direct application of the VBG. The key idea is that maximal two-body entanglement cannot be shared by a third party, which can be quantified by the CHSH score [49]. Although this method avoids imposing any assumptions on the measurement and transmission devices for security, a non-zero secure key rate can only be obtained when the entanglement of the transmitted state is sufficient, thus setting a threshold for transmission efficiency. Unfortunately, the theoretical lower bound for CHSH-based protocols [87] is far above the coupling limit imposed by the 3 dB atmosphere absorption using satellite-to-ground links [5].

We select the standard and simplest protocol for demonstration, which does not require any optimization of the experimental configuration but has a transmission efficiency threshold of $\eta_{\text{th}} \approx 90.8\%$ [54]. Analysis of other protocols can be conducted in a similar manner. The DI-QKD protocol consists of the following steps:

1. **State Distribution.** The source prepares a state of two photons in the following form:

$$\rho_s = V \cdot (|\Phi^-\rangle\langle\Phi^-|) + (1 - V) \cdot \frac{I}{2},$$

where $|\Phi^-\rangle = \frac{1}{\sqrt{2}}(|01\rangle - |10\rangle)$ is the singlet state and $V = \frac{4F-1}{3}$ denotes the visibility, with F being the fidelity of the state. Each photon is then

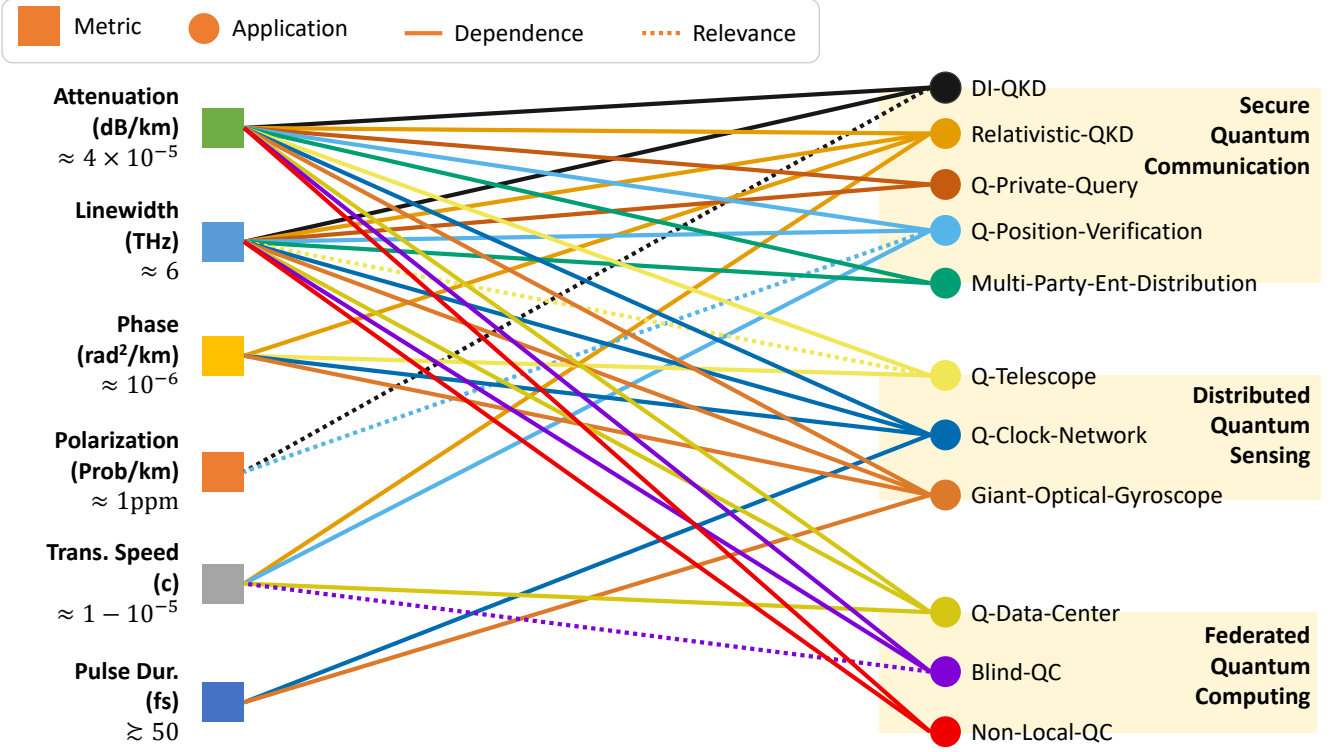


FIG. 3. Summary of VBG’s performance metrics and application requirements. The solid line indicates that the specific application depends on a certain performance metric, while the dotted line suggests that it may be relevant according to the concrete protocol. Here, the applications in the category of secure quantum computation include Device-Independent Quantum Key Distribution [49–57] (Sec. III A), Relativistic-QKD [31, 58] (Appendix. E 2), Quantum Private Query [59] (Appendix. E 2), Quantum Position Verification [60–62] (Appendix. E 1), and Multi-party Entangled State Distribution [63–67] (Appendix. E 2); Distributed quantum sensing covers Quantum Telescope [68–70] (Q-Telescope, Sec. III B), Quantum Clocks Network [71–73] (Appendix. E 3), and Giant Optical Gyroscope [74–76] (Appendix. E 4); And federated quantum computing consists of Quantum Data Centers [77, 78] (Appendix. E 5), Blind Quantum Computation [79, 80] (Sec. III C), and Non-Local Quantum Computation [81–83] (Appendix. E 6).

distributed to its respective party with an equal transmission efficiency of $\eta = 10^{-0.1\alpha L/2}$.

- Measurement.** Alice randomly chooses an input $x \in \{0, 1, 2\}$ and measures the state with the measurement operator $\hat{A}_x \in \{\sigma_z, (\sigma_z + \sigma_x)/\sqrt{2}, (\sigma_z - \sigma_x)/\sqrt{2}\}$. Similarly, Bob randomly chooses an input $y \in \{1, 2\}$ and measures the state with the measurement operator $\hat{B}_y \in \{\sigma_z, \sigma_x\}$. No-click events are assigned -1 for B_1, B_2, A_1, A_2 , but are assigned 0 for A_0 .

- Parameter Estimation.** Alice and Bob communicate to estimate the CHSH score,

$$S(\eta, F) \equiv \langle A_1(B_1 + B_2) + A_2(B_1 - B_2) \rangle. \quad (13)$$

- Privacy Amplification.** Alice uses measurement results A_0 to infer Bob’s key B_1 using hash function techniques. This step is done based on the value of S to first minimize the information that might leak and then maximize the correctness of the key.

Then, the key rate per single use of the channel can be calculated as [54]

$$r_{\text{DI-QKD}}(\eta, F) \geq 1 - h\left(\frac{1 + \sqrt{(S/2)^2 - 1}}{2}\right) - H(B_1|A_0), \quad (14)$$

where $h(x) = -x \log x - (1-x) \log(1-x)$ is the binary entropy function. The total key rate is given by integrating over the linewidth of the channels as

$$R_{\text{DI-QKD}} = \int r_{\text{DI-QKD}} d\nu \approx r_{\text{DI-QKD}}(\eta, F) \Delta\nu, \quad (15)$$

which has units of bits per second.

The achievable key rate for performing the DI-QKD protocol mentioned above, with a growing transmission distance, is shown with different generation fidelities in Fig. 4. With the achievable fidelity $F = 0.98$, the VBG can offer a Terabit per second key rate over a continental distance of 10^4 km, which can be further improved with a more advanced protocol. As DI-QKD protocols base

their security on the test of Bell-like inequalities, a practical scheme for DI-QKD also implies the feasibility of the fundamental loophole-free Bell test[88].

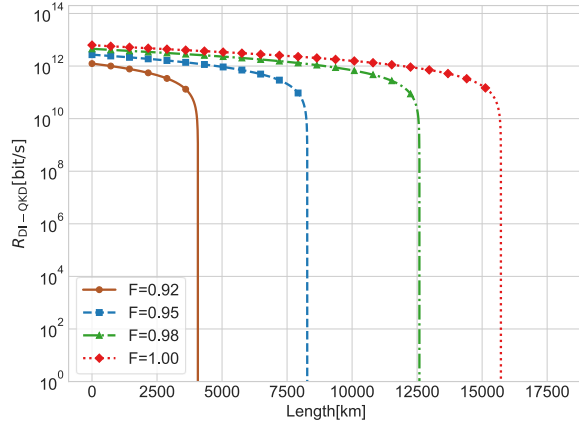


FIG. 4. DI-QKD key rate vs transmission distances using the VBG channel with different fidelities at generation.

B. Long Base-line Quantum Telescope

A Quantum Telescope (QTelescope) with a long baseline was proposed and theoretically shown to have quadratic precision enhancement in terms of source brightness ε for the astrometry of faint stellar objects that can be effectively treated as weak thermal sources [89]. An illustration of a basic model for a double-receiver long baseline quantum telescope [68–70] is shown in Fig. 5(a), where the incoming stellar light from both receivers is combined via the quantum channel to generate an interference pattern with a phase shift ϕ_0 , revealing the incoming angle information via $\phi_0 = \frac{2\pi L}{\lambda} \sin \theta$, with L being the baseline distance. Intuitively, the quantum telescope offers benefits over classical local schemes due to its ability to remove the position information of incoming photons by interference, thereby reducing uncertainty in momentum according to Heisenberg’s principle.

To quantitatively describe the astrometric performance, we estimate the uncertainty of θ in a single measurement with a time window τ for integration, which can be related to the uncertainty of ϕ_0 via the following simple error synthesis formula,

$$\sigma_\theta = \frac{\lambda}{2\pi L |\cos \theta|} \sigma_{\phi_0}. \quad (16)$$

In the direct interference scheme, ϕ_0 is encoded in the following state, which describes the incoming photon upon detection:

$$\rho_s = (1 - \varepsilon\eta)|00\rangle\langle 00| + \frac{\eta\varepsilon}{2} [|01\rangle\langle 01| + ge^{-\frac{1}{2}\sigma_\phi^2} e^{i\phi_0} |01\rangle\langle 10| + h.c.], \quad (17)$$

where η is again the transmission efficiency; $\sigma_\phi^2 \equiv \gamma L$ is the average dephasing in the transmission; g is the first-order correlation strength; and ε is the probability of containing a single photon from the incoming stellar wave packet. Using the Fisher information [90], we estimate the lower bound of the uncertainty using the corresponding POVM optimized photon detection over delay δ as

$$(\delta\theta \cdot |g| \cos \theta)^2 \geq \frac{\lambda^2}{4\pi^2 L^2} \frac{|g|}{F(\phi_0, \delta)} = A(\varepsilon, \lambda) \times \frac{e^{(\gamma+0.5\alpha)L}}{L^2}, \quad (18)$$

where $A(\varepsilon, \lambda) = \frac{\lambda^2}{4\pi^2 \varepsilon}$ is a pre-factor that depends on the source.

If there are no geographical constraints, the above equation reaches its minimum at $L = \frac{2}{\gamma+0.5\alpha}$ with a minimum value of $\frac{\lambda^2 e^{2(0.5\alpha+\gamma)}}{16\pi^2 \varepsilon}$. As a quantitative example, let $\tau \approx 0.01$ s be the atmospheric self-coherence time [91]. The loss, α , can be computed from Eq. (3) via a simple unit conversion. The probability is then found as $\varepsilon \approx \frac{\tau}{1_s} \approx 0.01$ for a stellar source in the H band with a magnitude of 24 (the limiting magnitude of automated all-sky astronomical surveys [92]). The relevant phase noise, $\gamma \approx 2 \int_0^{1/\tau} \hat{S}_\phi(f) \approx 10^{-6}$ rad²/km, is negligible compared to the attenuation.

The precision of the VBG scheme versus different baseline lengths, compared to the fiber scheme, is plotted in Fig. 5(b), which demonstrates a clear advantage of the VBG channel. At the scale of 10^3 km, the quantum telescopes can reach a precision approaching the milli-arcsecond level. However, the optimal baseline length is beyond 10^4 km, where the main limitation will be the Earth’s curvature.

C. Blind Delegated Quantum Computation

For delegating quantum computing tasks to the cloud, clients can transmit the entire quantum circuit and fetch outcomes using solely classical communication, assuming that both the input and output are classical. Nevertheless, when computations involve sensitive data or commercial confidentiality, clients may wish to conceal this information from the server while still utilizing its quantum capabilities. This motivates the investigation of blind quantum computation (BQC) [79]. Two principal strategies exist for achieving BQC: the pioneering universal BQC protocol [93] involves clients obfuscating their commands to ensure that only the circuit size can be leaked; alternatively, quantum private query techniques can be applied to include decoy instructions, thereby identifying deceitful servers with high certainty [94]. This discussion will concentrate on the first method, which ingeniously leverages measurement-based quantum computation (MBQC).

The primary aim is to achieve private quantum computation for a classical client. However, existing methods still require the client to perform at least some basic

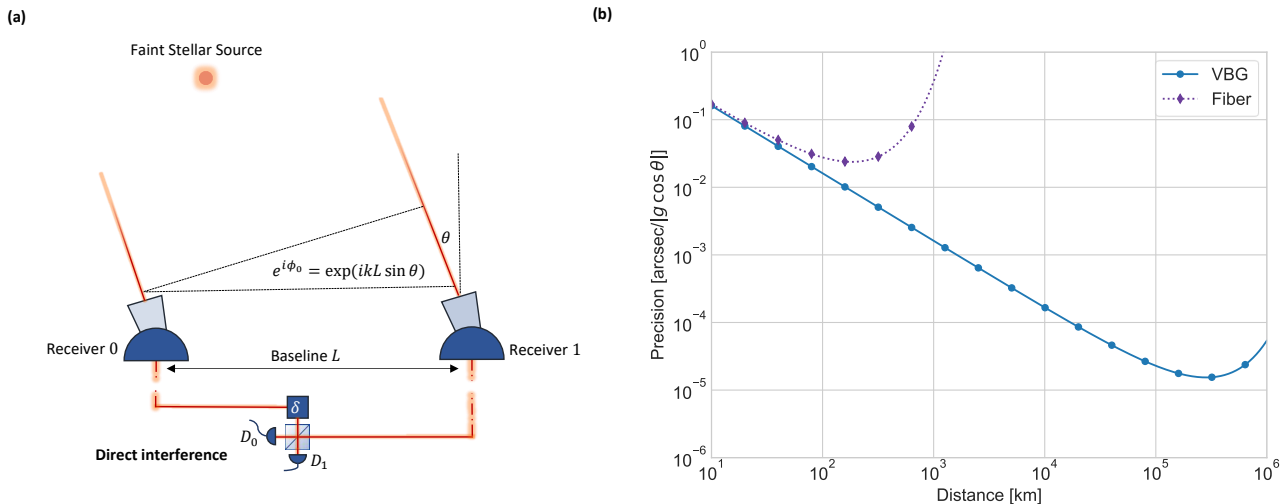


FIG. 5. Illustration and performance of a Quantum Telescope. (a) The light from both telescope stations is directly interfered to eliminate the position information. D_i is the photon detector. (b) Astrometric precision bounded by Fisher information for VBG and fiber, assuming different schemes for an H-band magnitude 24 stellar object under a single atmosphere coherent period (2×10^{-3} arcseconds ≈ 10 nrad.)

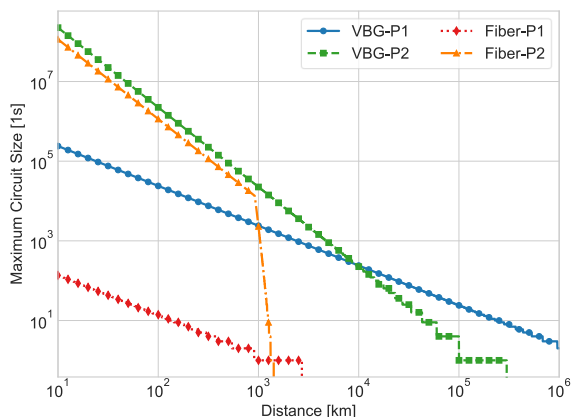


FIG. 6. The maximum circuit size assuming linear depth scaling that can be executed within one second versus distance between server and client under the direct measurement protocol (P1) and the heralded Bell pair protocol (P2) for fiber and VBG.

quantum operations, as fully classical clients with a single quantum server imply a non-trivial connection between BQP and NP. If clients can conduct arbitrary single-qubit measurements, the protocol becomes remarkably simple yet highly secure [80]. The client simply asks the server to prepare the required resource state for MBQC. The qubits are then sent to the client for adaptive measurement. Throughout this process, the no-signaling theorem [95] ensures that the client does not expose any computational details. Despite the significant advantages, its

main limitation is its vulnerability to loss. Consider a quantum circuit using an M -qubit resource state executed with a single-qubit coupling efficiency η ; the worst-case success probability is $P_{\text{success}} = \eta^M$. Although the VBG can achieve high coupling efficiency over continental distances, the growth of circuit size is still hindered by exponential decay, as illustrated in Fig. 6. The fiber can only support a circuit size of 10 qubits at an urban scale, while in comparison, computations involving 10^4 qubits across thousands of kilometers are feasible with the VBG, exceeding current quantum computations. Thus, transmission loss might not be the main limitation. Moreover, quantum error correction techniques, standard in quantum computing [96, 97], can mitigate the exponential decay of the success probability.

Another possible solution [80] is to utilize quantum teleportation with heralding, where the server sends half of the Bell pair to the client and requires the client to acknowledge receipt. In particular, the client can immediately perform the necessary measurement once the Bell pair is successfully received, without forwarding the measurement results to the server. This technique eliminates the requirement for quantum memory, as in the previous case. Therefore, the expected number of qubits sent from the server now scales as $\frac{M}{\eta}$. However, this protocol requires quantum non-demolition measurement techniques to herald [98] and sacrifices some security for the sake of loss tolerance, as extra communication between the server and the client may allow for a storage attack [99]. Another serious issue is that the execution time of a depth d will now be limited by the communication time $\tau_r = L/c$ between them. Assuming that the resources are properly allocated so that at least one Bell

pair is established for each qubit in a single round, the minimum execution time is limited by $\max\left(\frac{N}{\eta R_B}, \tau_c\right)d$, where R_B is the maximum Bell pair transmission rate under ideal multiplexing, and N is the number of qubits in a single layer. This is because the measurement results of the previous layer of the circuit from the server still need to be fed into the next layer and cannot be executed in parallel. The performance of this protocol under VBG, assuming linear depth growth, is also shown in Fig. 6 compared to the previous one. Although the heralded protocol is free from exponential decay and thus performs better than the previous one on a continental scale, it is noted that the former method gains advantages when the communication delay is significant. This disadvantage will become more pronounced when the depth of the circuit establishes super-linear scaling, which is common in fault-tolerant quantum computation [100, 101].

IV. DISCUSSION

In this work, we propose a simple prototype control system and construct a detailed model of the VBG channel for bosonic quantum information. A more detailed description of channel loss and linewidth is based on previous work [10], taking into account the topography of the Earth and reflective configurations to circumvent it. We also derive the full phase noise PSD characterizing the interference stability of the VBG device, quantitatively referring to the realistic parameters and experimental performance of the LIGO system [24, 102], which shows an RMS phase noise of $\sim 10^{-3}\text{rad}/\sqrt{\text{km} \cdot \text{Hz}}$ after active subtraction. Moreover, we analyze the resilience of VBG polarization using Kraus operators and evaluate the transmission delay and wave packet spreading influenced by dispersion effects, which are crucial for applications related to relativity.

Theoretical and numerical studies indicate notable improvements in the performance of various quantum protocols with the use of a VBG. In secure quantum communication, the VBG allows current DI-QKD protocols to function with today's technology, maintaining channel attenuation below the thresholds over continental spans. The ability of the VBG to transmit quantum signals with high accuracy between distant detectors enhances precision in applications such as quantum telescopes and other distributed sensing tasks. In network quantum computing, the strong establishment of quantum entanglement supports blind delegated computations over thousands of kilometers, using circuits with over 10^3 qubits.

Simultaneously with the creation of the analytical model in this study, detailed simulations using Finesse3 or equivalent optical tools [103, 104] are being conducted

to provide a precise depiction and rigorously evaluate the efficiency of VBG systems. Considering the projected expansion of VBG across continents, it is essential to integrate transient, significant environmental disturbances into the analysis to ensure sufficient redundancy for operational durability and longevity. The performance evaluation will proceed by implementing the system at full scale and collecting empirical data using the methods employed in LIGO [105, 106]. Small-scale tests using former LIGO experimental tubes are also currently being pursued.

Beyond the applications proposed and analyzed in this work, the VBG can be integrated with all-photonics repeaters [107–109] to establish a quantum network that theoretically possesses unlimited scale, facilitates the execution of a Bell test experiment with cognitive observers to examine the basic measurement assumption [110], and supports quantum holographic tasks [111]. The VBG may also provide cross-disciplinary advantages, including facilitating the long-range transmission of light bullets [112, 113], directly interconnecting multiple LIGO detectors as a potential central component of the anticipated Einstein telescope [114], and extending worldwide to perform large-scale geodesy measurements [115].

ACKNOWLEDGMENTS

We thank J.C Diels, Ming Lai, Ming Li, Kaushik Seshadreesan, Allen Zang, and Haiqi Zhou for their helpful discussions. This paper describes objective technical results and analysis. This research is supported by ARO(W911NF-23-1-0077), ARO MURI (W911NF-21-1-0325), AFOSR MURI (FA9550-19-1-0399, FA9550-21-1-0209, FA9550-23-1-0338), DARPA (HR0011-24-9-0359, HR0011-24-9-0361), NSF (OMA-1936118, ERC-1941583, OMA-2137642, OSI-2326767, CCF-2312755), NTT Research, Packard Foundation (2020-71479), and the Marshall and Arlene Bennett Family Research Program. U.S. Department of Energy, Office of Science, National Quantum Information Science Research Centers and Advanced Scientific Computing Research (ASCR) program (DE-AC02-06CH11357) and Oak Ridge Leadership Computing Facility (DE-AC05-00OR22725). National Science Foundation (Grant No. DMS-1929348). University of Pittsburgh, School of Computing and Information, Department of Computer Science, Pitt Cyber, Pitt Momentum Fund, PQI Community Collaboration Awards, John C. Mascaró Faculty Scholar in Sustainability, and Cisco Research. RXA would like to acknowledge support by the Woodnext Foundation as well as the Templeton Foundation. Any subjective views or opinions that might be expressed in the paper do not necessarily represent the views of the U.S. Department of Energy or the United States Government.

-
- [1] M. Petrovich, E. N. Fokoua, Y. Chen, H. Sakr, A. I. Adamu, R. Hassan, D. Wu, R. F. Ando, A. Papadimopoulos, S. R. Sandoghchi, *et al.*, First broadband optical fibre with an attenuation lower than 0.1 decibel per kilometre, arXiv preprint arXiv:2503.21467 (2025).
- [2] E. Numkam Fokoua, S. Abokhamis Mousavi, G. T. Jasion, D. J. Richardson, and F. Poletti, Loss in hollow-core optical fibers: mechanisms, scaling rules, and limits, *Advances in Optics and Photonics* **15**, 1 (2023).
- [3] H. Sakr, T. D. Bradley, G. T. Jasion, E. N. Fokoua, S. R. Sandoghchi, I. A. Davidson, A. Taranta, G. Guerra, W. Shere, Y. Chen, *et al.*, Hollow core nanfs with five nested tubes and record low loss at 850, 1060, 1300 and 1625nm, in *Optical Fiber Communication Conference* (Optica Publishing Group, 2021) pp. F3A–4.
- [4] M. Aspelmeyer, H. R. Bohm, T. Gyatso, T. Jennewein, R. Kaltenbaek, M. Lindenthal, G. Molina-Terriza, A. Poppe, K. Resch, M. Taraba, *et al.*, Long-distance free-space distribution of quantum entanglement, *science* **301**, 621 (2003).
- [5] C.-Y. Lu, Y. Cao, C.-Z. Peng, and J.-W. Pan, Micius quantum experiments in space, *Reviews of Modern Physics* **94**, 035001 (2022).
- [6] S. Goswami and S. Dhara, Satellite-relayed global quantum communication without quantum memory, *Physical Review Applied* **20**, 024048 (2023).
- [7] J. Yin, Y. Cao, Y.-H. Li, S.-K. Liao, L. Zhang, J.-G. Ren, W.-Q. Cai, W.-Y. Liu, B. Li, H. Dai, *et al.*, Satellite-based entanglement distribution over 1200 kilometers, *Science* **356**, 1140 (2017).
- [8] S.-K. Liao, W.-Q. Cai, W.-Y. Liu, L. Zhang, Y. Li, J.-G. Ren, J. Yin, Q. Shen, Y. Cao, Z.-P. Li, *et al.*, Satellite-to-ground quantum key distribution, *Nature* **549**, 43 (2017).
- [9] S. Muralidharan, L. Li, J. Kim, N. Lütkenhaus, M. D. Lukin, and L. Jiang, Optimal architectures for long distance quantum communication, *Scientific reports* **6**, 20463 (2016).
- [10] Y. Huang, F. Salces-Carcoba, R. X. Adhikari, A. H. Safavi-Naeini, and L. Jiang, Vacuum beam guide for large scale quantum networks, *Physical Review Letters* **133**, 020801 (2024).
- [11] A. S. Holevo and R. F. Werner, Evaluating capacities of bosonic gaussian channels, *Physical Review A* **63**, 032312 (2001).
- [12] K. Noh, V. V. Albert, and L. Jiang, Quantum capacity bounds of gaussian thermal loss channels and achievable rates with Gottesman-Kitaev-Preskill codes, *IEEE Transactions on Information Theory* **65**, 2563 (2018).
- [13] C.-H. Wang, F. Li, and L. Jiang, Quantum capacities of transducers, *Nature Communications* **13**, 6698 (2022).
- [14] M. Takeoka, S. Guha, and M. M. Wilde, Fundamental rate-loss tradeoff for optical quantum key distribution, *Nature communications* **5**, 5235 (2014).
- [15] P. Leviant, Q. Xu, L. Jiang, and S. Rosenblum, Quantum capacity and codes for the bosonic loss-dephasing channel, *Quantum* **6**, 821 (2022).
- [16] G. Zheng, W. He, G. Lee, K. Noh, and L. Jiang, Performance and achievable rates of the Gottesman-Kitaev-Preskill code for pure-loss and amplification channels, arXiv preprint arXiv:2412.06715 (2024).
- [17] Y. Zhang and T. Jennewein, Criteria for optimal entanglement-assisted long baseline imaging protocols, arXiv preprint arXiv:2501.16670 (2025).
- [18] S. D. Bartlett, T. Rudolph, and R. W. Spekkens, Reference frames, superselection rules, and quantum information, *Reviews of Modern Physics* **79**, 555 (2007).
- [19] W. J. Riley and D. A. Howe, *Handbook of frequency stability analysis*, Vol. 1065 (US Department of Commerce, National Institute of Standards and Technology . . . , 2008).
- [20] W. P. Robins, *Phase noise in signal sources: theory and applications*, Vol. 9 (IET, 1984).
- [21] D. V. Martynov, E. Hall, B. Abbott, R. Abbott, T. Abbott, C. Adams, R. Adhikari, R. Anderson, S. Anderson, K. Arai, *et al.*, Sensitivity of the advanced LIGO detectors at the beginning of gravitational wave astronomy, *Physical Review D* **93**, 112004 (2016).
- [22] A. Buikema, C. Cahillane, G. Mansell, C. Blair, R. Abbott, C. Adams, R. Adhikari, A. Ananyeva, S. Appert, K. Arai, *et al.*, Sensitivity and performance of the advanced LIGO detectors in the third observing run, *Physical Review D* **102**, 062003 (2020).
- [23] E. Capote, W. Jia, N. Aritomi, M. Nakano, V. Xu, R. Abbott, I. Abouelfettouh, R. Adhikari, A. Ananyeva, S. Appert, *et al.*, Advanced LIGO detector performance in the fourth observing run, *Physical Review D* **111**, 062002 (2025).
- [24] J. Aasi, B. Abbott, R. Abbott, T. Abbott, M. Abernathy, K. Ackley, C. Adams, T. Adams, P. Addesso, R. Adhikari, *et al.*, Advanced LIGO, *Classical and quantum gravity* **32**, 074001 (2015).
- [25] S. Pirandola, R. Laurenza, C. Ottaviani, and L. Banchi, Fundamental limits of repeaterless quantum communications, *Nature communications* **8**, 15043 (2017).
- [26] G. Zheng, W. He, G. Lee, K. Noh, and L. Jiang, Performance and achievable rates of the Gottesman-Kitaev-Preskill code for pure-loss and amplification channels, *PRX Quantum* **6**, 030314 (2025).
- [27] M. Subramanian, G. Zheng, and L. Jiang, Achievable rates for concatenated square Gottesman-Kitaev-Preskill codes, *PRX Quantum* **6**, 040342 (2025).
- [28] D. Gottesman, A. Kitaev, and J. Preskill, Encoding a qubit in an oscillator, *Physical Review A* **64**, 012310 (2001).
- [29] A. L. Grimsmo and S. Puri, Quantum error correction with the Gottesman-Kitaev-Preskill code, *PRX Quantum* **2**, 020101 (2021).
- [30] M. Lucamarini, Z. L. Yuan, J. F. Dynes, and A. J. Shields, Overcoming the rate-distance limit of quantum key distribution without quantum repeaters, *Nature* **557**, 400 (2018).
- [31] M. Sandfuchs, M. Haberland, V. Vilasini, and R. Wolf, Security of differential phase shift QKD from relativistic principles, *Quantum* **9**, 1611 (2025).
- [32] S. Wang, Z.-Q. Yin, D.-Y. He, W. Chen, R.-Q. Wang, P. Ye, Y. Zhou, G.-J. Fan-Yuan, F.-X. Wang, W. Chen, *et al.*, Twin-field quantum key distribution over 830-km fibre, *Nature Photonics* **16**, 154 (2022).
- [33] Y. Mao, P. Zeng, and T.-Y. Chen, Recent advances on quantum key distribution overcoming the linear secret key capacity bound, *Advanced Quantum Technologies*

- 4, 2000084 (2021).
- [34] R. Nehra, C. Oh, L. Jiang, and A. Marandi, All-optical loss-tolerant distributed quantum sensing, arXiv preprint arXiv:2407.13654 (2024).
- [35] A. Zang, A. Kolar, A. Gonzales, J. Chung, S. K. Gray, R. Kettimuthu, T. Zhong, and Z. H. Saleem, Quantum advantage in distributed sensing with noisy quantum networks, arXiv preprint arXiv:2409.17089 (2024).
- [36] S. M. Foreman, K. W. Holman, D. D. Hudson, D. J. Jones, and J. Ye, Remote transfer of ultrastable frequency references via fiber networks, *Review of Scientific Instruments* **78** (2007).
- [37] D. Shoemaker *et al.*, Advanced ligo reference design, LIGO Report **60056** (2009).
- [38] M. Evans, P. Fritschel, D. McClelland, J. Miller, A. Mullavey, D. Shaddock, B. Slagmolen, S. Waldman, *et al.*, Advanced ligo arm length stabilisation system design, LIGO Report **900144** (2009).
- [39] R. Abbott, R. Adhikari, G. Allen, S. Cowley, E. Daw, D. DeBra, J. Giaime, G. Hammond, M. Hammond, C. Hardham, *et al.*, Seismic isolation for advanced ligo, *Classical and Quantum Gravity* **19**, 1591 (2002).
- [40] F. Matchard, B. Lantz, R. Mittleman, K. Mason, J. Kissel, B. Abbott, S. Biscans, J. McIver, R. Abbott, S. Abbott, *et al.*, Seismic isolation of advanced ligo: Review of strategy, instrumentation and performance, *Classical and Quantum Gravity* **32**, 185003 (2015).
- [41] R. E. Bartolo, A. B. Tveten, and A. Dandridge, Thermal phase noise measurements in optical fiber interferometers, *IEEE Journal of Quantum Electronics* **48**, 720 (2012).
- [42] K. H. Wanser, Fundamental phase noise limit in optical fibres due to temperature fluctuations, *Electronics letters* **28**, 53 (1992).
- [43] L. Duan, Intrinsic thermal noise of optical fibres due to mechanical dissipation, *Electronics letters* **46**, 1515 (2010).
- [44] Y. Michimura, H. Wang, F. Salces-Carcoba, C. Wipf, A. Brooks, K. Arai, and R. X. Adhikari, Effects of mirror birefringence and its fluctuations to laser interferometric gravitational wave detectors, *Physical Review D* **109**, 022009 (2024).
- [45] E. Hirose, G. Billingsley, L. Zhang, H. Yamamoto, L. Pinard, C. Michel, D. Forest, B. Reichman, and M. Gross, Characterization of core optics in gravitational-wave detectors: Case study of kagra sapphire mirrors, *Physical Review Applied* **14**, 014021 (2020).
- [46] L. Pinard, C. Michel, B. Sassolas, L. Balzarini, J. Degallaix, V. Dolique, R. Flamini, D. Forest, M. Granata, B. Lagrange, *et al.*, Mirrors used in the ligo interferometers for first detection of gravitational waves, *Applied optics* **56**, C11 (2017).
- [47] J.-C. Diels and W. Rudolph, *Ultrashort laser pulse phenomena* (Elsevier, 2006).
- [48] Y. Arosa and R. de la Fuente, Refractive index spectroscopy and material dispersion in fused silica glass, *Optics Letters* **45**, 4268 (2020).
- [49] A. K. Ekert, Quantum cryptography based on bell's theorem, *Physical review letters* **67**, 661 (1991).
- [50] A. Acín, N. Brunner, N. Gisin, S. Massar, S. Pironio, and V. Scarani, Device-independent security of quantum cryptography against collective attacks, *Physical Review Letters* **98**, 230501 (2007).
- [51] L. Masanes, S. Pironio, and A. Acín, Secure device-independent quantum key distribution with causally independent measurement devices, *Nature communications* **2**, 238 (2011).
- [52] U. Vazirani and T. Vidick, Fully device independent quantum key distribution, *Communications of the ACM* **62**, 133 (2019).
- [53] R. Arnon-Friedman, F. Dupuis, O. Fawzi, R. Renner, and T. Vidick, Practical device-independent quantum cryptography via entropy accumulation, *Nature communications* **9**, 459 (2018).
- [54] P. Sekatski, J.-D. Bancal, X. Valcarce, E. Y.-Z. Tan, R. Renner, and N. Sangouard, Device-independent quantum key distribution from generalized chsh inequalities, *Quantum* **5**, 444 (2021).
- [55] W. Zhang, T. van Leent, K. Redeker, R. Garthoff, R. Schwonnek, F. Fertig, S. Eppelt, W. Rosenfeld, V. Scarani, C. C.-W. Lim, *et al.*, A device-independent quantum key distribution system for distant users, *Nature* **607**, 687 (2022).
- [56] F. Xu, Y.-Z. Zhang, Q. Zhang, and J.-W. Pan, Device-independent quantum key distribution with random postselection, *Physical review letters* **128**, 110506 (2022).
- [57] V. Zapatero, T. van Leent, R. Arnon-Friedman, W.-Z. Liu, Q. Zhang, H. Weinfurter, and M. Curty, Advances in device-independent quantum key distribution, *npj quantum information* **9**, 10 (2023).
- [58] K. Kravtsov, I. Radchenko, S. Kulik, and S. Molotkov, Relativistic quantum key distribution system with one-way quantum communication, *Scientific reports* **8**, 6102 (2018).
- [59] V. Giovannetti, S. Lloyd, and L. Maccone, Quantum private queries, *Physical review letters* **100**, 230502 (2008).
- [60] H. Buhrman, N. Chandran, S. Fehr, R. Gelles, V. Goyal, R. Ostrovsky, and C. Schaffner, Position-based quantum cryptography: Impossibility and constructions, *SIAM Journal on Computing* **43**, 150 (2014).
- [61] A. Bluhm, M. Christandl, and F. Speelman, A single-qubit position verification protocol that is secure against multi-qubit attacks, *Nature Physics* **18**, 623 (2022).
- [62] R. Allerstorfer, A. Bluhm, H. Buhrman, M. Christandl, L. Escolà-Farràs, F. Speelman, and P. V. Lunel, Making existing quantum position verification protocols secure against arbitrary transmission loss, arXiv preprint arXiv:2312.12614 (2023).
- [63] A. Fischer and D. Towsley, Distributing graph states across quantum networks, in *2021 IEEE International Conference on Quantum Computing and Engineering (QCE)* (IEEE, 2021) pp. 324–333.
- [64] C. Meignant, D. Markham, and F. Grosshans, Distributing graph states over arbitrary quantum networks, *Physical Review A* **100**, 052333 (2019).
- [65] X. Fan, C. Zhan, H. Gupta, and C. Ramakrishnan, Optimized distribution of entanglement graph states in quantum networks, *IEEE Transactions on Quantum Engineering* (2025).
- [66] Y. Huang, X. Ren, B. Li, Y. Wong, Z. Liang, and L. Jiang, Peer-to-peer distribution of graph states across spacetime quantum networks of arbitrary topology, *Proceedings of the ACM on Measurement and Analysis of Computing Systems* **9**, 1 (2025).
- [67] X. Fan, Y. Yang, H. Gupta, and C. Ramakrishnan, Distribution and purification of entanglement states in

- quantum networks, in *2025 International Conference on Quantum Communications, Networking, and Computing (QCNC)* (IEEE, 2025) pp. 74–82.
- [68] E. T. Khabiboulline, J. Borregaard, K. De Greve, and M. D. Lukin, Quantum-assisted telescope arrays, *Physical review A* **100**, 022316 (2019).
- [69] E. T. Khabiboulline, J. Borregaard, K. De Greve, and M. D. Lukin, Optical interferometry with quantum networks, *Physical review letters* **123**, 070504 (2019).
- [70] D. Gottesman, T. Jennewein, and S. Croke, Longer-baseline telescopes using quantum repeaters, *Physical review letters* **109**, 070503 (2012).
- [71] V. Giovannetti, S. Lloyd, and L. Maccone, Quantum-enhanced positioning and clock synchronization, *Nature* **412**, 417 (2001).
- [72] P. Komar, E. M. Kessler, M. Bishof, L. Jiang, A. S. Sørensen, J. Ye, and M. D. Lukin, A quantum network of clocks, *Nature Physics* **10**, 582 (2014).
- [73] V. Giovannetti, S. Lloyd, and L. Maccone, Positioning and clock synchronization through entanglement, *Physical Review A* **65**, 022309 (2002).
- [74] A. J. Brady and S. Haldar, Frame dragging and the hong-ou-mandel dip: Gravitational effects in multiphoton interference, *Physical Review Research* **3**, 023024 (2021).
- [75] F. Giovannetti, C. Altucci, F. Bajardi, A. Basti, N. Beverini, S. Capozziello, G. Carelli, S. Castellano, D. Ciampini, G. Di Somma, *et al.*, Gingerino: A high sensitivity ring laser gyroscope for fundamental and quantum physics investigation, *Frontiers in Quantum Science and Technology* **3**, 1363409 (2024).
- [76] A. D. Di Virgilio, F. Bajardi, A. Basti, N. Beverini, G. Carelli, D. Ciampini, G. Di Somma, F. Fuso, E. Maccioni, P. Marsili, *et al.*, Noise level of a ring laser gyroscope in the femto-rad/s range, *Physical Review Letters* **133**, 013601 (2024).
- [77] J. Liu, C. T. Hann, and L. Jiang, Data centers with quantum random access memory and quantum networks, *Physical Review A* **108**, 032610 (2023).
- [78] J. Liu and L. Jiang, Quantum data center: Perspectives, *IEEE Network* (2024).
- [79] J. F. Fitzsimons, Private quantum computation: an introduction to blind quantum computing and related protocols, *npj Quantum Information* **3**, 23 (2017).
- [80] T. Morimae and K. Fujii, Blind quantum computation protocol in which alice only makes measurements, *Physical Review A* **87**, 050301 (2013).
- [81] H. Buhrman, R. Cleve, S. Massar, and R. De Wolf, Nonlocality and communication complexity, *Reviews of modern physics* **82**, 665 (2010).
- [82] A. C.-C. Yao, Quantum circuit complexity, in *Proceedings of 1993 IEEE 34th Annual Foundations of Computer Science* (IEEE, 1993) pp. 352–361.
- [83] G. Brassard, Quantum communication complexity, *Foundations of Physics* **33**, 1593 (2003).
- [84] G. S. Ravi, K. N. Smith, P. Gokhale, and F. T. Chong, Quantum computing in the cloud: Analyzing job and machine characteristics, in *2021 IEEE International Symposium on Workload Characterization (IISWC)* (IEEE, 2021) pp. 39–50.
- [85] S. Wehner, D. Elkouss, and R. Hanson, Quantum internet: A vision for the road ahead, *Science* **362**, eaam9288 (2018).
- [86] S. J. Devitt, Performing quantum computing experiments in the cloud, *Physical Review A* **94**, 032329 (2016).
- [87] J.-Å. Larsson and J. Semitecolos, Strict detector-efficiency bounds for n-site clauser-horne inequalities, *Physical Review A* **63**, 022117 (2001).
- [88] M. Giustina, M. A. Versteegh, S. Wengerowsky, J. Handsteiner, A. Hochrainer, K. Phelan, F. Steinlechner, J. Kofler, J.-Å. Larsson, C. Abellán, *et al.*, A significant-loophole-free test of bell’s theorem with entangled photons, in *Quantum Information Science and Technology III*, Vol. 10442 (SPIE, 2017) pp. 19–27.
- [89] M. Tsang, Quantum nonlocality in weak-thermal-light interferometry, *Physical review letters* **107**, 270402 (2011).
- [90] B. R. Frieden and R. A. Gatenby, Principle of maximum fisher information from hardy’s axioms applied to statistical systems, *Physical Review E* **88**, 042144 (2013).
- [91] S. Lacour, F. Eisenhauer, S. Gillessen, O. Pfuhl, J. Woillez, H. Bonnet, G. Perrin, B. Lazareff, S. Rabien, V. Lapeyrere, *et al.*, Reaching micro-arcsecond astrometry with long baseline optical interferometry-application to the gravity instrument, *Astronomy & Astrophysics* **567**, A75 (2014).
- [92] N. Kaiser, H. Aussel, B. E. Burke, H. Boesgaard, K. Chambers, M. R. Chun, J. N. Heasley, K.-W. Hodapp, B. Hunt, R. Jedicke, *et al.*, Pan-starrs: a large synoptic survey telescope array, in *Survey and Other Telescope Technologies and Discoveries*, Vol. 4836 (SPIE, 2002) pp. 154–164.
- [93] A. Broadbent, J. Fitzsimons, and E. Kashefi, Universal blind quantum computation, in *2009 50th annual IEEE symposium on foundations of computer science* (IEEE, 2009) pp. 517–526.
- [94] V. Giovannetti, L. Maccone, T. Morimae, and T. G. Rudolph, Efficient universal blind quantum computation, *Physical review letters* **111**, 230501 (2013).
- [95] A. Peres and D. R. Terno, Quantum information and relativity theory, *Reviews of Modern Physics* **76**, 93 (2004).
- [96] S. D. Barrett and T. M. Stace, Fault tolerant quantum computation with very high threshold for loss errors, *Physical review letters* **105**, 200502 (2010).
- [97] Q. Xu, J. P. Bonilla Ataides, C. A. Pattison, N. Raveendran, D. Bluvstein, J. Wurtz, B. Vasić, M. D. Lukin, L. Jiang, and H. Zhou, Constant-overhead fault-tolerant quantum computation with reconfigurable atom arrays, *Nature Physics* **20**, 1084 (2024).
- [98] K. Xia, M. Johnsson, P. L. Knight, and J. Twamley, Cavity-free scheme for nondestructive detection of a single optical photon, *Physical review letters* **116**, 023601 (2016).
- [99] J. Barrett, R. Colbeck, and A. Kent, Memory attacks on device-independent quantum cryptography, *Physical review letters* **110**, 010503 (2013).
- [100] H. Yamasaki and M. Koashi, Time-efficient constant-space-overhead fault-tolerant quantum computation, *Nature Physics* **20**, 247 (2024).
- [101] S. Tamiya, M. Koashi, and H. Yamasaki, Polylog-time-and constant-space-overhead fault-tolerant quantum computation with quantum low-density parity-check codes, *arXiv preprint arXiv:2411.03683* (2024).
- [102] B. Abbott, R. Abbott, R. Adhikari, P. Ajith, B. Allen, G. Allen, R. Amin, S. Anderson, W. Anderson, M. Arain, *et al.*, Ligo: the laser interferometer

- gravitational-wave observatory, Reports on Progress in physics **72**, 076901 (2009).
- [103] P. Maheshwari, Ligo surf 2024: Interim report ii—vacuum beam guide for quantum communication, LIGO Report (2024).
- [104] H. Rose, Analysis of a vacuum beam guide for quantum communications, LIGO Report (2024).
- [105] P. Nguyen, R. Schofield, A. Effler, C. Austin, V. Adya, M. Ball, S. Banagiri, K. Banowetz, C. Billman, C. Blair, *et al.*, Environmental noise in advanced ligo detectors, Classical and Quantum Gravity **38**, 145001 (2021).
- [106] J. Kruk and R. Schofield, Environmental monitoring: Coupling function calculator (2016).
- [107] K. Azuma, K. Tamaki, and H.-K. Lo, All-photonic quantum repeaters, Nature communications **6**, 1 (2015).
- [108] Y. Gan, M. Azari, N. K. Chandra, X. Jin, J. Cheng, K. P. Seshadreesan, and J. Liu, Quantum repeaters enhanced by vacuum beam guides, arXiv preprint arXiv:2504.13397 (2025).
- [109] D. Fuentealba, J. Dahn, J. Steck, and E. Behrman, Robust and scalable quantum repeaters using machine learning, Preprints 10.20944/preprints202505.0691.v1 (2025).
- [110] J. S. Bell, *Speakable and unspeakable in quantum mechanics: Collected papers on quantum philosophy* (Cambridge university press, 2004).
- [111] A. May, Quantum tasks in holography, Journal of High Energy Physics **2019**, 1 (2019).
- [112] C. Guo, M. Xiao, M. Orenstein, and S. Fan, Structured 3d linear space–time light bullets by nonlocal nanophotonics, Light: Science & Applications **10**, 160 (2021).
- [113] A. Chong, W. H. Renninger, D. N. Christodoulides, and F. W. Wise, Airy–bessel wave packets as versatile linear light bullets, Nature photonics **4**, 103 (2010).
- [114] S. Kroker and R. Nawrodt, The einstein telescope, in *2014 IEEE Metrology for Aerospace (MetroAeroSpace)* (IEEE, 2014) pp. 288–292.
- [115] J. Li, E. Biondi, E. R. Heimisson, S. Puel, Q. Zhai, S. Zhang, V. Hjörleifsdóttir, X. Wei, E. Bird, A. Klesh, *et al.*, Minute-scale dynamics of recurrent dike intrusions in iceland with fiber-optic geodesy, Science **388**, 1189 (2025).
- [116] F. J. Sánchez-Sesma, R. L. Weaver, H. Kawase, S. Matsushima, F. Luzón, and M. Campillo, Energy partitions among elastic waves for dynamic surface loads in a semi-infinite solid, Bulletin of the Seismological Society of America **101**, 1704 (2011).
- [117] S. Stein and M. Wyssession, *An introduction to seismology, earthquakes, and earth structure* (John Wiley & Sons, 2009).
- [118] P. M. Shearer, *Introduction to seismology* (Cambridge university press, 2019).
- [119] J. W. Goodman, *Introduction to Fourier optics* (Roberts and Company publishers, 2005).
- [120] G. Mueller, Beam jitter coupling in advanced ligo, Optics Express **13**, 7118 (2005).
- [121] D. Z. Anderson, Alignment of resonant optical cavities, Applied Optics **23**, 2944 (1984).
- [122] L. Barsotti, M. Evans, and P. Fritschel, Alignment sensing and control in advanced ligo, Classical and Quantum Gravity **27**, 084026 (2010).
- [123] B. Canuel, E. Genin, M. Mantovani, J. Marque, P. Ruggi, and M. Tacca, Sub-nanoradiant beam pointing monitoring and stabilization system for controlling input beam jitter in gravitational wave interferometers, Applied Optics **53**, 2906 (2014).
- [124] Minus K Technology, Transmissibility curves for vibration isolation tables, platforms, isolators & systems: Performance (n.d.), section “CM-1 Isolator”.
- [125] D. Thomas, V. Mohit, and C. Christophe, Complementary filters shaping using \mathcal{H}_∞ synthesis, in *2019 7th International Conference on Control, Mechatronics and Automation (ICCMA)* (IEEE, 2019) pp. 459–464.
- [126] C. M. Harris and A. G. Piersol, *Harris’ shock and vibration handbook*, Vol. 5 (McGraw-Hill New York, 2002).
- [127] A. Downey and L. Micheli, Vibration mechanics: A practical introduction for mechanical, civil, and aerospace engineers, OSF (2025).
- [128] T. L. Schmitz and K. S. Smith, *Mechanical vibrations* (Springer, 2012).
- [129] H. Jia, J. Yang, and X. Li, Minimum variance unbiased subpixel centroid estimation of point image limited by photon shot noise, Journal of the Optical Society of America A **27**, 2038 (2010).
- [130] R. E. Thompson, D. R. Larson, and W. W. Webb, Precise nanometer localization analysis for individual fluorescent probes, Biophysical journal **82**, 2775 (2002).
- [131] R. J. Ober, S. Ram, and E. S. Ward, Localization accuracy in single-molecule microscopy, Biophysical journal **86**, 1185 (2004).
- [132] C. S. Smith, N. Joseph, B. Rieger, and K. A. Lidke, Fast, single-molecule localization that achieves theoretically minimum uncertainty, Nature methods **7**, 373 (2010).
- [133] S. M. Foreman, A. D. Ludlow, M. H. De Miranda, J. E. Stalnaker, S. A. Diddams, and J. Ye, Coherent optical phase transfer over a 32-km fiber with 1 s instability at 10-17, Physical Review Letters **99**, 153601 (2007).
- [134] The tilting will introduce a lateral shift of the transmitted beam that leads to a dispersion separation of the AUX beam (1600 nm) and the signal beam (~ 1550 nm). However, the separation induced by each lens is less than 1 nm, and thus the effects are trivial.
- [135] In principle, the reflected beam can also be extracted at each lens or coupled into a stabilized fiber for routing back to the mirror node. We only aim to provide one possible solution here, while the engineering team will decide on the best strategy upon deployment.
- [136] G. De Vine, D. A. Shaddock, B. Ware, R. E. Spero, D. M. Wuchenich, W. M. Klipstein, and K. McKenzie, *High-Speed Digital Interferometry*, Tech. Rep. (NASA, 2012).
- [137] K. Izumi, K. Arai, B. Barr, J. Betzwieser, A. Brooks, K. Dahl, S. Doravari, J. C. Driggers, W. Z. Korth, H. Miao, *et al.*, Multicolor cavity metrology, Journal of the Optical Society of America A **29**, 2092 (2012).
- [138] R. W. Drever, J. L. Hall, F. V. Kowalski, J. Hough, G. Ford, A. Munley, and H. Ward, Laser phase and frequency stabilization using an optical resonator, Applied Physics B **31**, 97 (1983).
- [139] This scaling assumption is pessimistic, as the system will be buried 2-meters under the ground, which can result in exponential suppression of ground excited high-frequency seismic and acoustic noises due to dirt attenuation.
- [140] J. Hough, S. Rowan, and B. S. Sathyaprakash, The search for gravitational waves, Journal of Physics B: Atomic, Molecular and Optical Physics **38**, S497 (2005).
- [141] R. E. Anthony, A. T. Ringler, and D. C. Wilson, Seismic

- background noise levels across the continental united states from usarray transportable array: The influence of geology and geography, *Bulletin of the Seismological Society of America* **112**, 646 (2022).
- [142] D. G. Albert and S. N. Decato, Acoustic and seismic ambient noise measurements in urban and rural areas, *Applied Acoustics* **119**, 135 (2017).
- [143] M. P. Ross, K. Venkateswara, C. Mow-Lowry, S. Cooper, J. Warner, B. Lantz, J. Kissel, H. Radkins, T. Shaffer, R. Mittleman, *et al.*, Towards windproofing ligo: reducing the effect of wind-driven floor tilt by using rotation sensors in active seismic isolation, *Classical and Quantum Gravity* **37**, 185018 (2020).
- [144] J. R. Peterson, *Observations and modeling of seismic background noise*, Tech. Rep. (US Geological Survey, 1993).
- [145] A. Brotzer, H. Igel, E. Stutzmann, J.-P. Montagner, F. Bernauer, J. Wassermann, R. Widmer-Schmidrig, C.-J. Lin, S. Kiselev, F. Vernon, *et al.*, Characterizing the background noise level of rotational ground motions on earth, *Seismological Research Letters* **95**, 1858 (2024).
- [146] R. Soomro, C. Weidle, L. Cristiano, S. Lebedev, T. Meier, and P. W. Group, Phase velocities of rayleigh and love waves in central and northern europe from automated, broad-band, interstation measurements, *Geophysical Journal International* **204**, 517 (2016).
- [147] R. A. Williams, W. J. Stephenson, J. K. Odum, and D. M. Worley, *High-resolution surface-seismic imaging techniques for NEHRP soil profile classifications and earthquake hazard assessments in urban areas*, Tech. Rep. (US Geological Survey; Branch of Information Services [distributor],, 1997).
- [148] The near-surface seismic/acoustic angular noises are mainly attributed to Rayleigh waves, shear waves, and love waves [116], among which the Rayleigh wave speed is the slowest and roughly equals $c_{s,\text{Rayleigh}} \approx 0.9c_{s,\text{shear}} \approx 270 \text{ m/s}$ [117, 118].
- [149] K. U. Schreiber, G. E. Stedman, H. Igel, and A. Flaws, Ring laser gyroscopes as rotation sensors for seismic wave studies, in *Earthquake source asymmetry, structural media and rotation effects* (Springer, 2006) pp. 377–390.
- [150] J. Giaime, B. Lantz, C. Hardham, W. Hua, R. Adhikari, D. DeBra, G. Hammond, M. Hammond, J. How, S. Richman, *et al.*, Advanced ligo seismic isolation system conceptual design, LIGO document E **10016** (2001).
- [151] R. Weiss, Mitscattering by residual gas https://dcc.ligo.org/public/0028/t890025/001_T890025-01.pdf (1989).
- [152] A. Cumming, A. Bell, L. Barsotti, M. Barton, G. Cagnoli, D. Cook, L. Cunningham, M. Evans, G. Hammond, G. Harry, *et al.*, Design and development of the advanced ligo monolithic fused silica suspension, *Classical and Quantum Gravity* **29**, 035003 (2012).
- [153] G. M. Harry, A. M. Gretarsson, P. R. Saulson, S. E. Kitelberger, S. D. Penn, W. J. Startin, S. Rowan, M. M. Fejer, D. Crooks, G. Cagnoli, *et al.*, Thermal noise in interferometric gravitational wave detectors due to dielectric optical coatings, *Classical and Quantum Gravity* **19**, 897 (2002).
- [154] A. Amato, G. Cagnoli, M. Granata, B. Sassolas, J. Degallaix, D. Forest, C. Michel, L. Pinard, N. Demos, S. Gras, *et al.*, Optical and mechanical properties of ion-beam-sputtered nb 2 o 5 and tio 2-nb 2 o 5 thin films for gravitational-wave interferometers and an improved measurement of coating thermal noise in advanced ligo, *Physical Review D* **103**, 072001 (2021).
- [155] K. Somiya, Thermal noise of geo’s beamsplitter, LIGO Report (2009).
- [156] S. Dwyer and S. W. Ballmer, Radiative thermal noise for transmissive optics in gravitational-wave detectors, *Physical Review D* **90**, 043013 (2014).
- [157] B. Benthem and Y. Levin, Thermorefractive and thermochemical noise in the beamsplitter of the geo600 gravitational-wave interferometer, *Physical Review D* **80**, 062004 (2009).
- [158] F. Bielsa, A. Dupays, M. Fouché, R. Battesti, C. Robilliard, and C. Rizzo, Birefringence of interferential mirrors at normal incidence: Experimental and computational study, *Applied Physics B* **97**, 457 (2009).
- [159] M. Kitagawa and M. Tateda, Form birefringence of sio2/ta2o5 periodic multilayers, *Applied optics* **24**, 3359 (1985).
- [160] K. Kraus, A. Böhm, J. D. Dollard, and W. Wootters, *States, Effects, and Operations Fundamental Notions of Quantum Theory: Lectures in Mathematical Physics at the University of Texas at Austin* (Springer, 1983).
- [161] L. E. Kinsler, A. R. Frey, A. B. Coppens, and J. V. Sanders, *Fundamentals of acoustics* (John wiley & sons, 2000).
- [162] M. Greenspan, Propagation of sound in five monatomic gases, *The Journal of the Acoustical Society of America* **28**, 644 (1956).
- [163] E. Meyer and G. Sessler, Schallausbreitung in gasen bei hohen frequenzen und sehr niedrigen drucken, *Zeitschrift für Physik* **149**, 15 (1957).
- [164] J. C. Owens, Optical refractive index of air: dependence on pressure, temperature and composition, *Applied optics* **6**, 51 (1967).
- [165] S. L. Kramer and J. P. Stewart, *Geotechnical earthquake engineering* (CRC Press, 2024).
- [166] In fact, the actual effective attenuation will be larger as Rayleigh waves dominate the noise power near the surface, which suffers from strong geometric decay.
- [167] S. P. Francis, T. T. Lam, K. McKenzie, A. J. Sutton, R. L. Ward, D. E. McClelland, and D. A. Shaddock, Weak-light phase tracking with a low cycle slip rate, *Optics Letters* **39**, 5251 (2014).
- [168] Roughly 10 ppm of the 1 W AUX beam will be reflected, and we assume that 10 percent of its power will be collected as a conservative estimate.
- [169] D. Matei, T. Legero, S. Häfner, C. Grebing, R. Weyrich, W. Zhang, L. Sonderhouse, J. Robinson, J. Ye, F. Riehle, *et al.*, 1.5 μm lasers with sub-10 mhz linewidth, *Physical review letters* **118**, 263202 (2017).
- [170] C. Cahillane, *Controlling and calibrating interferometric gravitational wave detectors* (California Institute of Technology, 2021).
- [171] For the case of high input noise, f_c is chosen to be around 10 Hz to further suppress the low frequency noise. The actual loop delay is mainly limited by the actuator bandwidth, rather than the signal transmission delay.
- [172] P. M. Leung and T. C. Ralph, Quantum memory scheme based on optical fibers and cavities, *Physical Review A* **74**, 022311 (2006).
- [173] T. Pittman and J. Franson, Cyclical quantum mem-

- ory for photonic qubits, *Physical Review A* **66**, 062302 (2002).
- [174] F. B. Früngel, *Optical Pulses-Lasers-Measuring Techniques* (Academic Press, 2014).
- [175] Edmund Optics, Laser Line Polarizing Plate Beamsplitters (2025), product No. 39878; accessed July 3, 2025.
- [176] S. Feng and H. G. Winful, Physical origin of the gouy phase shift, *Optics letters* **26**, 485 (2001).
- [177] O. Svelto, D. C. Hanna, *et al.*, *Principles of lasers*, Vol. 1 (Springer, 2010).
- [178] Z. Chai, X. Hu, F. Wang, X. Niu, J. Xie, and Q. Gong, Ultrafast all-optical switching, *Advanced Optical Materials* **5**, 1600665 (2017).
- [179] N. R. Newbury, P. A. Williams, and W. C. Swann, Coherent transfer of an optical carrier over 251 km, *Optics letters* **32**, 3056 (2007).
- [180] K. Predehl, G. Grosche, S. Raupach, S. Droste, O. Terra, J. Alnis, T. Legero, T. Hänsch, T. Udem, R. Holzwarth, *et al.*, A 920-kilometer optical fiber link for frequency metrology at the 19th decimal place, *Science* **336**, 441 (2012).
- [181] M. Schioppo, J. Kronjaeger, A. Silva, R. Ilieva, J. Patterson, C. Baynham, W. Bowden, I. Hill, R. Hobson, A. Vianello, *et al.*, Comparing ultrastable lasers at 7×10^{-17} fractional frequency instability through a 2220 km optical fibre network, *Nature communications* **13**, 212 (2022).
- [182] S. Droste, F. Ozimek, T. Udem, K. Predehl, T. Hänsch, H. Schnatz, G. Grosche, and R. Holzwarth, Optical-frequency transfer over a single-span 1840 km fiber link, *Physical review letters* **111**, 110801 (2013).
- [183] B. P. Dix-Matthews, S. W. Schediwy, D. R. Gozzard, E. Savalle, F.-X. Esnault, T. Lévêque, C. Gravestock, D. D’Mello, S. Karpathakis, M. Tobar, *et al.*, Point-to-point stabilized optical frequency transfer with active optics, *Nature communications* **12**, 515 (2021).
- [184] N. Hoghooghi, M. Mazur, N. Fontaine, Y. Liu, D. Lee, C. McLemore, T. Nakamura, T. Hayashi, G. Di Sciullo, D. Shaji, *et al.*, Enabling a multifunctional telecommunications fiber optic network: Ultrastable optical frequency transfer and attosecond timing in deployed multicore fiber, *arXiv preprint arXiv:2410.13801* (2024).
- [185] S. Bregni and L. Primerano, Using the modified allan variance for accurate estimation of the hurst parameter of long-range dependent traffic, *arXiv preprint cs/0510006* (2005).
- [186] L. M. Ward and P. E. Greenwood, 1/f noise, *Scholarpedia* **2**, 1537 (2007), revision #137265.
- [187] N. Chandran, V. Goyal, R. Moriarty, and R. Ostrovsky, Position based cryptography, in *Annual International Cryptology Conference* (Springer, 2009) pp. 391–407.
- [188] S. Beigi and R. König, Simplified instantaneous non-local quantum computation with applications to position-based cryptography, *New Journal of Physics* **13**, 093036 (2011).
- [189] V. Asadi, R. Cleve, E. Culf, and A. May, Linear gate bounds against natural functions for position-verification, *Quantum* **9**, 1604 (2025).
- [190] J. Memmen, J. Eisert, and N. Walk, Advantage of multi-partite entanglement for quantum cryptography over long and short ranged networks, *arXiv preprint arXiv:2312.13376* (2023).
- [191] R. Cleve, D. Gottesman, and H.-K. Lo, How to share a quantum secret, *Physical review letters* **83**, 648 (1999).
- [192] M. Hillery, V. Bužek, and A. Berthiaume, Quantum secret sharing, *Physical Review A* **59**, 1829 (1999).
- [193] M. Hein, W. Dür, J. Eisert, R. Raussendorf, M. Van den Nest, and H.-J. Briegel, Entanglement in graph states and its applications, in *Quantum computers, algorithms and chaos* (IOS Press, 2006) pp. 115–218.
- [194] D. Markham and B. C. Sanders, Graph states for quantum secret sharing, *Physical Review A* **78**, 042309 (2008).
- [195] A. Einstein *et al.*, Zur elektrodynamik bewegter körper, *Annalen der physik* **17**, 891 (1905).
- [196] J. P. Covey, I. Pikovski, and J. Borregaard, Probing curved spacetime with a distributed atomic processor clock, *PRX Quantum* **6**, 030310 (2025).
- [197] P. Wcisło, P. Ablewski, K. Beloy, S. Bilicki, M. Bober, R. Brown, R. Fasano, R. Ciuryło, H. Hachisu, T. Ido, *et al.*, New bounds on dark matter coupling from a global network of optical atomic clocks, *Science Advances* **4**, eaau4869 (2018).
- [198] T. Takano, M. Takamoto, I. Ushijima, N. Ohmae, T. Akatsuka, A. Yamaguchi, Y. Kuroishi, H. Munekane, B. Miyahara, and H. Katori, Geopotential measurements with synchronously linked optical lattice clocks, *Nature Photonics* **10**, 662 (2016).
- [199] G. Sagnac, Sur la preuve de la réalité de l’éther lumineux par l’expérience de l’interférographe tournant, *CR Acad. Sci.* **157**, 1410 (1913).
- [200] H. Thirring, Über die wirkung rotierender ferner massen in der einsteinschen gravitationstheorie., *Physikalische Zeitschrift* **19**, 33 (1918).
- [201] A. Lyons, G. C. Knee, E. Bolduc, T. Roger, J. Leach, E. M. Gauger, and D. Faccio, Attosecond-resolution hong-ou-mandel interferometry, *Science advances* **4**, eaap9416 (2018).
- [202] L. Arissian and J.-C. Diels, Intracavity phase interferometry: frequency combs sensor inside a laser cavity, *Laser & Photonics Reviews* **8**, 799 (2014).
- [203] M. O. Scully, M. S. Zubairy, and M. Haugan, Proposed optical test of metric gravitation theories, *Physical Review A* **24**, 2009 (1981).
- [204] X. Zhu, M. Lenzner, and J.-C. Diels, Phase nanoscopy with correlated frequency combs, *Sensors* **23**, 301 (2022).
- [205] J.-C. M. Diels, X. Zhu, and M. Lenzner, Sub-nano-scale phase sensing and improvement by squeezing, in *Quantum Sensing, Imaging, and Precision Metrology* (SPIE, 2023) p. PC1244710.
- [206] V. Giovannetti, S. Lloyd, and L. Maccone, Quantum random access memory, *Physical review letters* **100**, 160501 (2008).
- [207] G. Brassard, H. Buhrman, N. Linden, A. A. Méthot, A. Tapp, and F. Unger, Limit on nonlocality in any world in which communication complexity is not trivial, *Physical Review Letters* **96**, 250401 (2006).
- [208] S. Popescu and D. Rohrlich, Quantum nonlocality as an axiom, *Foundations of Physics* **24**, 379 (1994).
- [209] B. S. Cirel’son, Quantum generalizations of bell’s inequality, *Letters in Mathematical Physics* **4**, 93 (1980).
- [210] D. Ding and L. Jiang, Coordinating decisions via quantum telepathy, *arXiv preprint arXiv:2407.21723* (2024).
- [211] A. Effler, P. Fritschel, E. Hall, and M. Landry, A roadmap for the ligo observatories in the era of cosmic explorer, *LIGO Report* (2023).

- [212] L. Datrier, G. Lovelace, J. R. Smith, A. Saenz, and A. Romero, Site evaluation and cost estimation for cosmic explorer, arXiv preprint arXiv:2509.05430 (2025).
- [213] S. C. Webb, Broadband seismology and noise under the ocean, *Reviews of Geophysics* **36**, 105 (1998).
- [214] K. Nishida, Ambient seismic wave field, *Proceedings of the Japan Academy, Series B* **93**, 423 (2017).
- [215] D. W. Allan, Should the classical variance be used as a basic measure in standards metrology?, *IEEE Transactions on Instrumentation and Measurement*, 646 (2012).
- [216] B. Lenoir, Predicting the variance of a measurement with 1/f noise, *Fluctuation and Noise Letters* **12**, 1350006 (2013).
- [217] LIGO Caltech, Vacuum, <https://www.ligo.caltech.edu/page/vacuum>.
- [218] J. Livas and B. Moore, Ligo vacuum system study, *The Journal of Environmental Sciences* **32**, 28 (1989).
- [219] J. F. O’Hanlon, *A user’s guide to vacuum technology* (John Wiley & Sons, 2003).
- [220] G. Billingsley, H. Yamamoto, and L. Zhang, Characterization of advanced ligo core optics, *American Society for Precision Engineering (ASPE)* **66**, 78 (2017).
- [221] J. Kraus, J. Davis, B. Rubin, O. Lyngnes, and A. Ode, Improving throughput of ion beam sputtered optical films, in *56th Annual Technical Conference Proceedings of the Society of Vacuum Coaters* (Society of Vacuum Coaters, Providence, RI, 2013) pp. 245–248.
- [222] H. Cui, B. Li, Y. Han, J. Wang, C. Gao, and Y. Wang, Simultaneous measurements of s-and p-polarization reflectivity with a cavity ring-down technique employing no polarization optics, *Chinese Optics Letters* **15**, 053101 (2017).
- [223] M. Granata, A. Amato, L. Balzarini, M. Canepa, J. Degallaix, D. Forest, V. Dolique, L. Mereni, C. Michel, L. Pinard, *et al.*, Amorphous optical coatings of present gravitational-wave interferometers, *Classical and Quantum Gravity* **37**, 095004 (2020).
- [224] J. Buchli, B. Tracey, T. Andric, C. Wipf, Y. H. J. Chiu, M. Lochbrunner, C. Donner, R. X. Adhikari, J. Harms, I. Barr, *et al.*, Improving cosmological reach of a gravitational wave observatory using deep loop shaping, *Science* **389**, 1012 (2025).

Appendix A: The VBG Control System

1. Overview of the Design

It is a trivial fact that if we simply replicate the control system design of LIGO for each VBG section, we can, in principle, arrive at a quantum channel that has excellent optical performance with existing techniques. However, this design comes with infeasible construction costs and complexity. Therefore, the main purpose of this section is to provide a prototype design that is as simple as possible while still being capable of realizing our performance claim. The realistic construction of VBG may not necessarily follow the prototype design here and can be improved and further simplified with careful and detailed engineering considerations, which are beyond the scope of this work.

The design of the VBG control system consists of the following three parts:

1. **Passive Isolation Platform (PIP)**. The nodes (lenses and mirrors) are rigidly mounted to passive isolation platforms. The platforms isolate the optics from the ground motion above ~ 1 Hz and follow the local ground motion below 1 Hz.
2. **Alignment Control System (ACS)**. The auxiliary sensing laser (AUX) beams are injected from both ends of the VBG and are co(counter)-propagated alongside the quantum information signal beam. The beam position on each lens and mirror is imaged by a camera. All of these positions are then recorded and used to control the angle of each of the steering mirrors (and possibly also the transverse alignment of the lenses).
3. **Section Length Stabilization (SLS)**. The AUX beam reflected at each section is extracted at the steering mirror node and mixed with the AUX beam reflected (transmitted) at the previous lens (mirror) to perform section-wise, round-trip heterodyne phase detection. The detected phase (beat) serves as the feedback signal for the SLS system to drive the actuators on the mirror to perform active control of the section length. The signal can also be used for post-subtraction only for applications that do not require real-time processing.

We remark that among the above systems, the PIP and SLS systems are required only to maintain the phase stability claim of the VBG systems, while ACS is crucial for maintaining all other performance metrics in Table. II.

2. Steering Mirrors

Due to the extended length of the VBG, it is necessary to deploy mirrors to deflect the beam to account for both the curvature of the Earth and man-made infrastructure above and below ground. This problem has been previously addressed in a satellite-based scheme [6]. In reality, the infrastructure issue is more serious and determines the number of required steering mirrors. A conservative estimation assumes the minimum use of a steering mirror every $L_{\text{mirror}} \sim 10$ km, which corresponds to roughly a maximum of 3 lens sections between two steering mirrors. Such a separation corresponds to a construction depth of $D \sim \frac{L_{\text{mirror}}^2}{8R_E} \sim 2$ m where $R_E \approx 6000$ km is the radius of the Earth. This result implies that the VBG system should be constructed on the Earth’s surface to avoid digging costs.

These steering mirrors will be accompanied by an alignment control sensing system to ensure that the light spot on each lens is within 0.1 mm of the reference optical axis defined by the center of the two neighboring mirrors, as shown in Fig. 7.

The loss induced by these steering mirrors can be estimated following a similar process as that for the lenses, which gives a similar requirement for the radius, coating, and translation alignment. However, the loss introduced by the angular misalignment, which is negligible in the lens case, may now become a serious problem and dominate the additional mirror loss. In our analysis, the static centers of neighboring mirrors defined the ground-truth reference optical axis. When referenced to this axis, the loss associated with each lens is dominated by its transverse displacement, while angular misalignment becomes the dominant source of loss for the mirrors.

To estimate the precision requirement, we consider a single-plane mirror with a typical incident angle of $\frac{\pi}{4}$ to deflect the beam and decompose the rotation into two independent DOFs, namely tipping $\delta\beta_s$ and tilting $\delta\beta_p$ with respect to the center point of the mirror. For the loss introduced by the tip, one can show by a simple argument on the solution of the Helmholtz equation and by rotating the optical axis for the plane mirror that the loss and phase shift depend only on the misalignment angle, regardless of its original orientation angle β_s [119]. This result allows us to consider only the case $\beta_s = 0$ so that the effects of tilt angle misalignment $\delta\beta_p$ can be converted into an effective tipping angle of $\delta\beta_s^{\text{eff}} \approx \frac{\sqrt{2}}{2}\delta\beta_p$.

Suppose that the mirror is located at z with respect to the beam waist. Then, using the conventional mode expansion method, the power leaked to the E_0^1 and E_0^{-1} Laguerre-Gaussian modes can be calculated as,

$$l_{\delta\beta_s} \approx k^2 w^2(z) \delta\beta_s^2 \sim \left(\frac{\delta\beta_s}{\beta_G}\right)^2, \quad (\text{A1})$$

where $\beta_G = \frac{\lambda}{\pi w(0)} \sim 10^{-5} \text{rad}$ is the divergence angle of the Gaussian beam, which agrees with the reference [120, 121]. One also finds that the loss is minimized when the mirror is placed at the waist. Then, we have

$$l_{\delta\beta_s} \approx \frac{2\pi L_0}{\lambda} \delta\beta^2. \quad (\text{A2})$$

For an order of magnitude estimate, plugging in $\delta\beta_s \approx 0.05 \mu\text{rad} \sim 0.5\% \beta_G$, one finds that $l_{\delta\beta_s} \approx 40 \text{ppm}$ for the default configuration, which corresponds to an angular misalignment well above the actuator precision employed in the advanced LIGO [122, 123]. An intuitive way to understand such a requirement is that the 0.1 mm displacement error corresponds to $\frac{0.1 \text{mm}}{2000 \text{m}} \approx 0.05 \mu\text{rad}$ rotational precision. In comparison, the loss induced by lens tilting is given by

$$l'_{\delta\beta} \approx \frac{2d^2}{w_0^2} \left(\frac{n-1}{n}\right)^2 \delta\beta^2 \sim 0.05 \delta\beta^2, \quad (\text{A3})$$

which implies that a tilting precision at the level of tens of milliradians will be sufficient, rendering this contribution negligible in our loss analysis.

3. Passive Isolation Platform

The vibration isolation system we assume is based on existing commercial solutions [124]. In this setup, the optical table acts as a rigid body isolated by pairs of parallel springs, as shown in Fig. 8 (a). Under the simple harmonic oscillator approximation, the transmissibility can be expressed as [125, 126]

$$T_z(f) = \sqrt{\frac{1 + \left(2\xi \frac{f}{f_n}\right)^2}{\left(1 - \left(\frac{f}{f_n}\right)^2\right)^2 + \left(2\xi \frac{f}{f_n}\right)^2}}, \quad (\text{A4})$$

where $\xi \approx 0.1$, $f_n \approx 0.5 \text{Hz}$ are the typical damping ratio and natural (resonant) frequency respectively for a commercial passive isolated optical table.

The transmissibility for the ground rotations can be estimated using a similar method by substituting the mass with the moment of inertia and the force with the torque, which leads to essentially the same expression, [127, 128]

$$T_\beta(f) = \sqrt{\frac{1 + \left(2\xi_\beta \frac{f}{f_{n,\beta}}\right)^2}{\left(1 - \left(\frac{f}{f_{n,\beta}}\right)^2\right)^2 + \left(2\xi_\beta \frac{f}{f_{n,\beta}}\right)^2}}, \quad (\text{A5})$$

with $\xi_\beta = \sqrt{3}\xi$, $f_{r,\beta} = \sqrt{3}f_r$ being the natural frequency and damping ratio for the rotation, respectively. The estimated transmissibility curve of the passive isolation and the corresponding measured data from a commercially available system are plotted in Fig. 8 (b), demonstrating good agreement with our prediction.

However, it should be noted that the simple harmonic oscillator approximation given by Eq.(A4)-(A5) fails at frequencies above $\gtrsim 100 \text{Hz}$ due to internal mode resonances of the springs and rigid bodies. To account for this behavior, we assume that the transmissibility becomes flat at high frequencies for a conservative estimate.

4. Alignment Control System

An auxiliary (AUX) laser at 1600nm is emitted at the beginning of the VBG and co-propagates with the quantum signal beam. The spot position of the emitted auxiliary laser is monitored by cameras at each node to provide an alignment error signal for the ACS system, as shown in Fig. 7. ACS aims to eliminate static and ultra-low frequency drift, and it is expected to function at a frequency below 0.01 Hz, implying that the measurements can be slow but must be precise. The measured displacement at each node serves as the feedback system to drive the actuators and actuators to control the rotational and translational alignment of the mirrors and lenses, so that the spots of sensing light can be locked to the centers of the mirrors and lenses within

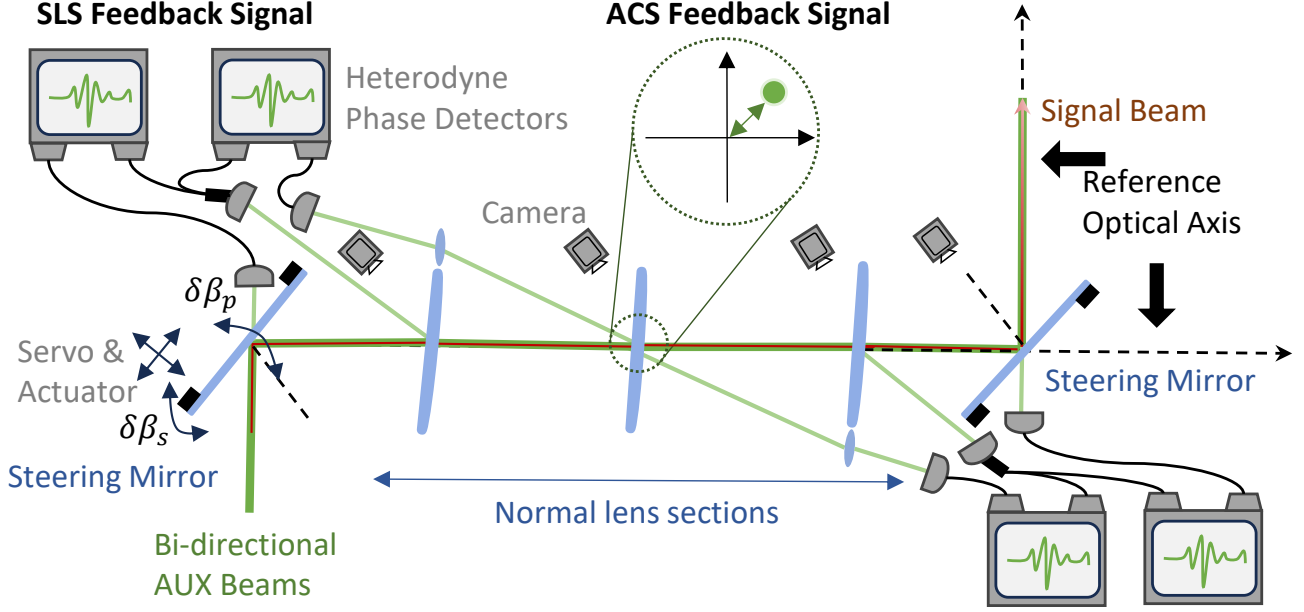


FIG. 7. The illustration of the steering mirrors, alignment control system (ACS) and the section length stabilization (SLS) system.

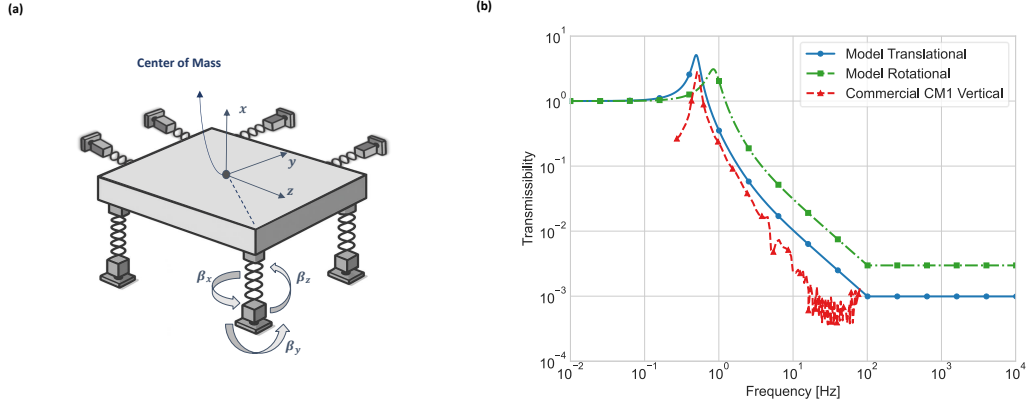


FIG. 8. The (a) illustration and the (b) performance of the PIP. The vertical isolation performance of the commercially available CM1 optical table [124] is also plotted for comparison.

an rms error tolerance of 0.08 mm. It is not hard to show by simple geometric optics that such a requirement corresponds to a transverse deviation of the lenses' centers from the reference axis with a maximum variance of $\delta s^2 \sim (0.1 \text{ mm})^2$ and a maximum mirror angular deviation variance of $\delta\beta^2 \sim (0.05 \text{ } \mu\text{rad})^2$.

As the required bandwidth is slow and the actuator precision is well above the requirement, the residual movement is essentially determined by the sensing noise. Determining the spot position is necessarily a centroid estimation problem, where the noise limit is given by

[129–131],

$$\frac{\delta x_s^2}{(w/2)^2} \sim \frac{1 + \frac{1}{3}(a/w)^2}{N_{ph}}, \quad (\text{A6})$$

where w is the spot size, a is the pixel size, and N_{ph} is the total number of received photons in one exposure. Experimental results with advanced CCD cameras and suitable analyzing algorithms demonstrate that the above noise limit can be achieved within a factor of three, provided that the required precision is no better than the nanometer scale [132]. For a conservative estimate, assume that the camera has $P \approx 1 \text{ nW}$ with $T = 100 \text{ ms}$ exposure time ($N_{ph} \sim 10^9$) and a negligible pixel size ($w \gg a$). Then,

the sensing noise floor is estimated to be $10^{-5}w$, which is two orders of magnitude smaller than our requirement. Thus, we expect the current design of the ACS system to work well beyond our requirement with an initial sensing laser power of 1 W and a scattering power of roughly $1 \mu\text{W}$ at each lens/mirror. Notably, the most analogous setup to ours involves the alignment of the input beam in LIGO, where the control system operates at normal pressure rather than under vacuum, achieves sub-micrometer alignment precision [123], and provides angular sensing precision at the sub-nanoradian level. The same system can also be adapted for our purposes in future upgrades, if necessary.

5. Section Length Stabilization

SLS is designed to suppress the phase noise below 10 Hz as the VBG itself is expected to be stable at high frequencies. To reduce system complexity, we propose reusing the reflected (transmitted) AUX beam generated by imperfect AR (HR) coatings, which would otherwise contribute to signal beam loss, to implement the standard round-trip phase cancellation technique that is widely employed in fiber for long-distance frequency transfer [133]. The AUX beam is locked to an ultra-stable laser or atomic clock at emission to provide a stable absolute length reference for the SLS.

To separate the reflected beam from the main optical path of the co-propagating AUX beam, the lenses' surfaces can be engineered such that the first surface is flat and tilted by an angle of $0.02 \sim 0.05 \text{ mrad}$ with respect to the reference optical axis, as shown in Fig. 7 [134]. This tilting will shift the spot of the reflected beam away from the center of the previous node by 20 cm. The required tilting alignment precision for each lens is only $\sim 0.01 \text{ mrad}$, corresponding to a transverse shift of $\sim 4 \text{ cm}$, which is readily achievable by monitoring the spot location using a fraction of the reflected beam, since we can tolerate a relatively large loss in the reflected beam.

The reflected beam is extracted at the steering mirror node [135]. Then, the beam from the closest lens is split into two, with one part being mixed with the transmitted beam from the lens and the other part being mixed with the reflected beam from the second closest lens using the heterodyne phase detector [136]. The SLS feedback signal, length fluctuation between the two steering mirrors, is calculated using the beat signals from the local detectors along with the results from the neighboring steering mirror node.

Finally, the feedback signal is low-pass filtered and used to drive the local mirror actuator to ensure that the mirror is following the movement of the previous one, thus actively stabilizing the section length below 10 Hz.

The noise budget analysis (Subsec. B6) suggests that such a simple SLS design is sufficient to achieve our performance claim. However, if a more complicated scheme

becomes necessary, one option is to inject an independent, ultra-stable SLS laser with a carefully selected wavelength at each steering mirror by engineering the steering mirrors to have higher transmissibility at that wavelength. Then, the multi-color arm length stabilization scheme [137] can be applied to lock the section length to the laser frequency using the PDH method [138]. Alternatively, a completely separate beam path could be used for the SLS sensing laser by attaching co-moving tiny lenses and mirrors to the main optical components of the VBG, at the expense of increased system complexity.

Appendix B: Details of Noise Budgets

In this section, we provide a detailed description of noise budgets for estimating the phase noise power spectral density, as shown in Fig. 9, utilizing a comparative and extrapolative method with the data and analysis from advanced LIGO [21–23].

1. Seismic and Alignment Noise

The seismic noise at the lens and mirror positions will introduce movement into the system and cause phase noise. Empirically, the phase noise is dominated by $k\delta z$, with δz being the parallel movement. However, rotational and translational movement may also couple into the phase noise due to static misalignment. Here, we will present a theoretical derivation based on the Laguerre-Gaussian mode expansion, which we have used to derive the loss for cross-verification. Then, we estimate the post-isolated phase noise contribution to the final noise power spectrum based on measured and theoretical seismic movements.

a. Lens Section

Parallel Movement. The movement of the lens parallel to the laser beam will not significantly affect phase noise, as the light is merely transmitted through the lens. By expanding the perturbed light field in the Laguerre-Gaussian basis (LG) and collecting the imaginary part of the fundamental mode, the leading contribution from the defocus effect (Gouy phase) can be identified as,

$$\delta\phi \sim \frac{\delta z}{L_0}, \quad (\text{B1})$$

which is greatly suppressed by the section length L_0 .

Transversal Displacement. Similarly, let δs denote the offset of the beam and expand the light field after a perturbed lens in the original LG basis. One finds that the phase shift (piston shift) is of the second order of δs

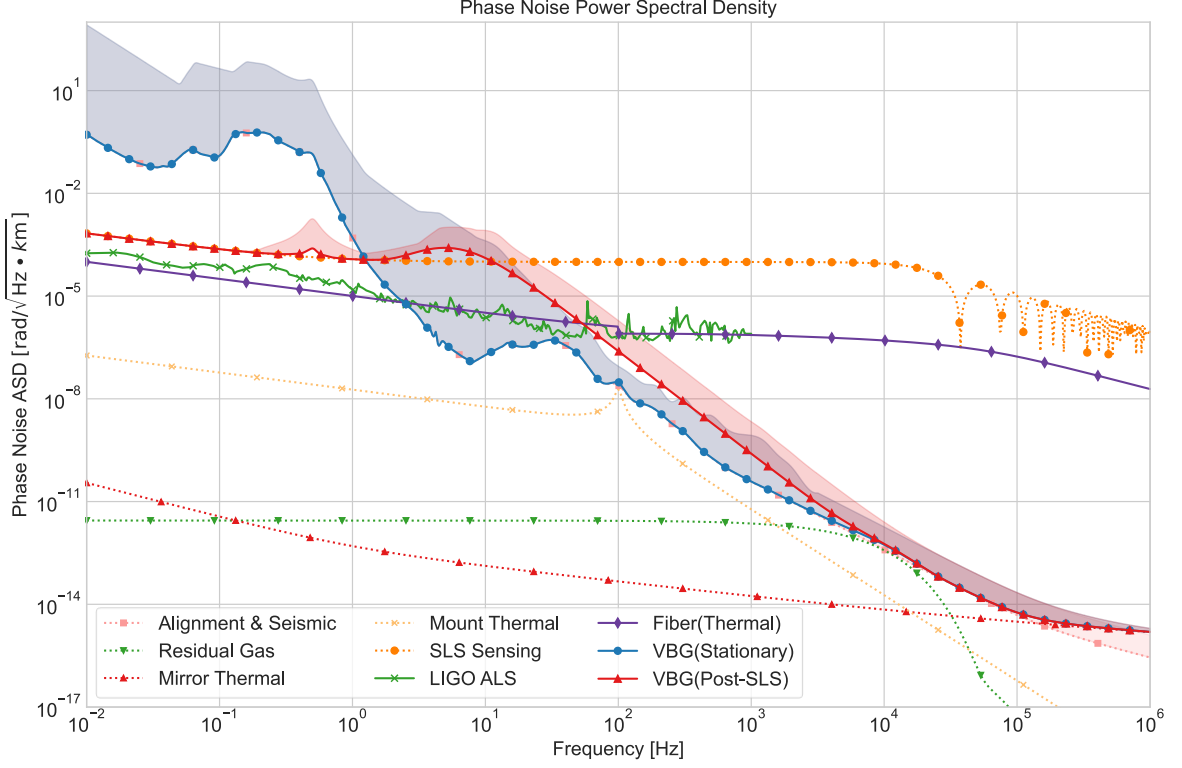


FIG. 9. Normalized phase noise amplitude spectral density of the VBG before and after SLS, optical fiber thermal noise [41–43], and the detailed noise budget. The upper edges of the shaded regions represent the corresponding noises (Alignment & Seismic, VBG before and post SLS) under the high seismic input case.

and is estimated as

$$\delta\phi \sim -k \frac{\delta s^2}{L_0}. \quad (\text{B2})$$

To include its contribution to the noise power spectrum, we can replace one of the δs with twice the expected static misalignment tolerance, $2\delta s_s \leq 0.2$ mm, which corresponds to a coupling factor of $2k \frac{\delta s_s}{L_0} \sim 5 \times 10^{-8} k$ that is expected to be negligible compared to the displacement noise introduced by the mirror.

Rotation. One can expect that the phase shift is of second order in $\delta\beta_{s/p}$. Following a simple geometric argument, the leading contribution is estimated to be

$$\delta\phi \approx \frac{k(n-1)d}{2n} \delta\beta_{s/p}^2, \quad (\text{B3})$$

with $d \approx 2$ cm being the thickness of the lens and n being the effective refractive index of the lens. Similarly, one can replace one of the $\delta\beta_{s/p}$ with twice the static tolerance value of $2\delta\beta_{s/p,s} \leq 0.02$ mrad to obtain a coupling factor of $\frac{k(n-1)d\delta\beta_{s/p,s}}{2n} \sim 120 \mu\text{m/rad}$.

b. Mirrors Section

Translation. For simplicity, we can assume the incident angle to be 0° for an order-of-magnitude esti-

mate. The parallel movement represents the strongest movement-to-phase coupling as

$$\delta\phi \sim 2k\delta z. \quad (\text{B4})$$

In contrast, the transversal movement (δs) does not impose any phase shift. The cross-coupling term, seen below, is greatly suppressed due to the high angular alignment control requirement for the mirror ($\sim 0.05 \mu\text{rad}$).

Rotation. Rotation itself only introduces pure loss, rather than a phase shift. However, it couples through the parallel movement as,

$$\delta\phi \sim 2k\delta s\delta\beta, \quad (\text{B5})$$

assuming the worst case scenario in which the transversal movement aligns with the rotation. With the same techniques, the coupling factor is estimated to be $200k \mu\text{m/rad}$.

c. Seismic Input

Generally, seismic-induced **translation** rolls off as $\delta z(f) \sim \frac{1}{f^2}$ [139], while establishing several peaks and long-term drift at low frequencies [140]. Therefore, to estimate the seismic-induced translation movement, we can

use the low-frequency measured data from the BSSA survey [141] and the high-frequency data of the urban and rural areas collected by ERDC-CRREL [142]. Then, we extrapolate the spectrum to high frequencies using the aforementioned $\frac{1}{f^2}$ scaling, which is shown in Fig. 10 (a) in comparison to the LIGO site data [40, 143]. Specifically, the median noise data from BSSA is combined with the rural area data to define the baseline phase stability of the VBG. This baseline is then used for all subsequent performance estimates, under the assumption that the VBG will be constructed and routed through relatively quiet regions where the LIGO data is representative of this noise level. For completeness, we also combine the high-noise model (NHNM) [144] with the urban residential region data to provide performance estimates in noisy environments, in which the noise level is roughly two to three orders of magnitude larger in the 3 – 30 Hz band.

As for the **rotation**, it can be estimated from the translational seismic movement [145].

By assuming a seismic wave propagating with displacement $z(x, t)$, we can calculate the induced tilting as

$$\delta\beta(x, t) = \frac{\partial z(x, t)}{\partial x} \approx kz. \quad (\text{B6})$$

Therefore, the PSD of the tilting can be calculated from the PSD of the seismic-induced translation as

$$S_\beta(f) \approx k^2 S_z(f) \approx \left(\frac{2\pi f}{c_s}\right)^2 S_z(f), \quad (\text{B7})$$

where c_s is the speed of the seismic wave. At low frequencies, the seismic wave speed is determined by the hard bedrock and can reach 2 ~ 3 km/s [118, 146], whereas at higher frequencies, the wave speed is significantly slower because the waves are trapped by the shallow soil layer, with typical values ranging from ~ 100 m/s to ~ 800 m/s. We take a typical value of $c_{s, \text{shear}} \sim 300$ m/s [147] [148]. The tilting input data used in the following calculation, obtained from the theoretical models described above, are plotted in Fig. 10 (b) and compared with the LIGO data and the Wettzell measurement data [143, 149]. The LIGO data is found to be at a similar level to the low noise model and is approximately an order of magnitude larger than the Wettzell measurements, which is likely due to extra tilting induced by the wind. Because the system will be buried, we may neglect the wind induced motion, and thus our model provides a conservative estimate. In fact, the tilting induced phase noise is roughly 3 to 4 orders of magnitude smaller than the translational induced phase noise and never exceeds 10^{-5} rad rms, even in the high noise case, which means its contribution is trivial and can be safely neglected.

As seen later, the performance of the VBG is acceptable even in a high-noise and unlikely environment after the engagement of the SLS system, which demonstrates the robustness of the control system design. However, the rms angular motion after the PIP system, integrated across the spectrum, in the high-noise case is approxi-

mately $0.1 \mu\text{rad}$, which is two times larger than our assumed maximum mirror angular deviation. As a result, the ACS system must operate with a faster bandwidth (≥ 0.5 Hz) in high-noise environments to ensure stable system performance. Alternatively, a more expensive and advanced isolation platform [39, 150] can be employed in particularly noisy areas when necessary, depending on practical engineering considerations.

2. Residual Gas Noise

The default residual gas pressure in the VBG is ~ 1 Pascal, which is approximately seven orders of magnitude higher than that of LIGO. In addition to the finite transmissibility of acoustic noise, the statistical fluctuation in the effective index of refraction of the low pressure gas introduces a phase noise floor for the VBG that extends up to tens of kilohertz.

Under thermal equilibrium, interactions between gas molecules and the propagating light introduce scattering phase noise, which is dominated by forward scattering and can be estimated by [151]

$$\delta\phi = \frac{(2\pi)^2 \alpha \sqrt{\rho_\# L_0}}{\lambda \sqrt{w_0 v_0}} e^{-\sqrt{2\pi} \frac{f w_0}{v_0}}, \quad (\text{B8})$$

where α is the molecular polarizability, $\rho_\#$ is the particle number density, v_0 is the thermal velocity of the gas, and w_0 is the average radius of the beam. And for our configuration, assuming N_2 is dominating, we have

$$\delta\phi \sim 10^{-11} \times \left(\frac{1550 \text{ nm}}{\lambda}\right)^{\frac{5}{4}} \sqrt{\frac{P}{1 \text{ Pa}}} e^{-\frac{f}{5 \text{ kHz}}} \text{ rad}/\sqrt{\text{Hz}}. \quad (\text{B9})$$

In addition to nitrogen, hydrogen and helium should also be considered, as they have a cutoff frequency an order of magnitude larger than that of N_2 and may therefore dominate the residual gas scattering noise above 100 kHz. Their contributions have also been included in the final noise budget, assuming volume ratios of 1 ppm and 10 ppm, respectively.

3. Thermal Noise

The thermal noise mainly comes from the rigid mount holding the steering mirrors and the internal thermal noise of the mirrors themselves.

For the **mounts**, the thermal noise can be estimated by applying the fluctuation-dissipation theorem for the damped harmonic oscillator model as [152],

$$\delta\phi = \sqrt{\frac{4k_B T}{2\pi m f \lambda^2} \left(\frac{f_0^2/Q}{f_0^4/Q^2 + (f_0^2 - f^2)^2} \right)}, \quad (\text{B10})$$

where $f_0 \sim 100$ Hz, $Q \sim 10$, and $m \approx 2$ kg are the typical eigenfrequencies, quality factors, and total masses (in-

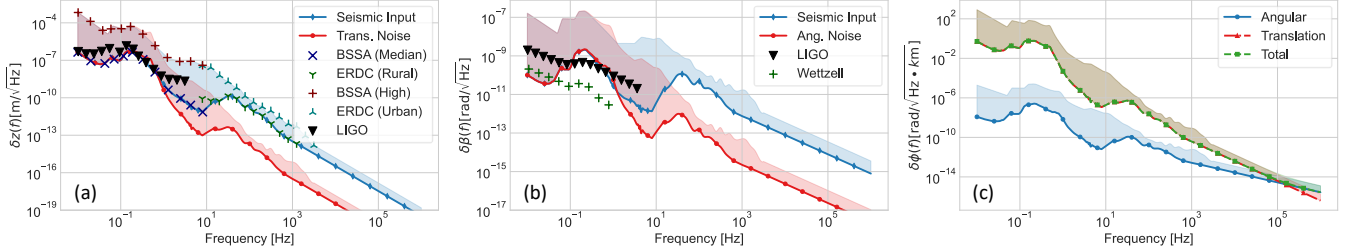


FIG. 10. The noise ASD of the seismic input, passive isolated platform and their contributions to the final PNASD. The upper edge of the corresponding shaded regions represents the noises under high seismic input. (a) Translation movement ASD. (b) Rotation movement ASD. (c) The expected contribution to PNASD.

cluding mirrors/lenses), respectively, for a conservative estimate.

As for the **mirror** noise, it may include Brownian noise and thermo-optic noise for both the substrate and the coating. Assuming that we use the same materials for the substrate and coating as LIGO, the thermal noise for the mirror will be dominated by the coating Brownian noise, which can be calculated using the fluctuation-dissipation theorem as [153]

$$\delta\phi = \frac{2\pi}{\lambda} \sqrt{\frac{2k_B T d_c}{\pi^2 f w^2 Y} \left(\frac{Y'}{Y} \phi_{\parallel} + \frac{Y}{Y'} \phi_{\perp} \right)}, \quad (\text{B11})$$

where w is the beam radius at the mirror, ϕ_{\parallel} and ϕ_{\perp} are the parallel and orthogonal loss angles of the coating, Y and Y' are the Young's moduli for the substrate and the coating, and d_c is the thickness of the coating. Using the values from LIGO, an order of magnitude estimate is found as [154]

$$\delta\phi_{BN,c} \sim 1 \times 10^{-12} \left(\frac{1550 \text{ nm}}{\lambda} \right)^{3/2} \left(\frac{1 \text{ Hz}}{f} \right)^{0.45} \text{ rad}/\sqrt{\text{Hz}}. \quad (\text{B12})$$

For the **lenses**, the thermal noise budgets for transmissive optics differ from those for reflective ones. Providing an exact and detailed estimate of the thermal noise is impossible due to a lack of knowledge about the material properties. Here, we only estimate the bulk transmissive noise for the substrates, which is likely the dominant noise, and adapt the values from the reflective optics case to serve as our order of magnitude estimate based on the following reasons [155]:

1. For the Brownian noises, their values are largely determined by the loss angles, which are unknown unless a real measurement is performed. However, the mechanism of Brownian noise does not depend on whether the light is reflected or transmitted; instead, it merely depends on the material structure and properties. For coating, the noise scales as $\frac{d_c}{w^2}$, with d_c being the thickness of the coating and w

being the waist of the beam. Considering that the AR coating is roughly an order of magnitude thinner than the HR coating being used in LIGO, it is very likely that the coating Brownian noises will be smaller in the AR case.

2. For the thermal-optics noise of the coating, the PSD also scales linearly with the thickness. Therefore, if the same material is being used, it is reasonable to believe that the thermal-optic noise will be smaller in the AR case.

For the lens' substrate, the bulk transmission thermal-optic noise can be calculated as [156, 157]

$$S_x^{TO}(f) = \frac{16k_B \kappa T^2 \beta_{eff}^2 d}{\pi C^2 \rho^2 w^4 \omega^2}, \quad (\text{B13})$$

where $\beta_{eff} = \frac{dn}{dT} + \alpha(n-1)$ is the effective thermal response, $d \sim 2\text{cm}$ is the thickness of the substrate, and other parameters are defined as before but for the substrate. Then, the thermal-optic noise for the substrate can be numerically estimated as

$$\delta\phi_{TO,s}(f) \sim 2 \times 10^{-12} \left(\frac{1 \text{ Hz}}{f} \right) \left(\frac{1550 \text{ nm}}{\lambda} \right)^2. \quad (\text{B14})$$

The thermal noise budget, including all relevant components, is shown in Fig. 11. We observe that the substrate thermal-optic noise dominates at low frequencies, while the coating Brownian noise dominates at high frequencies.

4. Birefringence Noise

Birefringence in both the substrate and the coating not only degrades polarization stability but can also couple to phase noise when the orientation of the optic axis of an optical component is perturbed relative to the polarization of the signal light. The analysis from LIGO recently addresses this issue in a coherent way [44], since they have a cavity with light bouncing back and forth. We

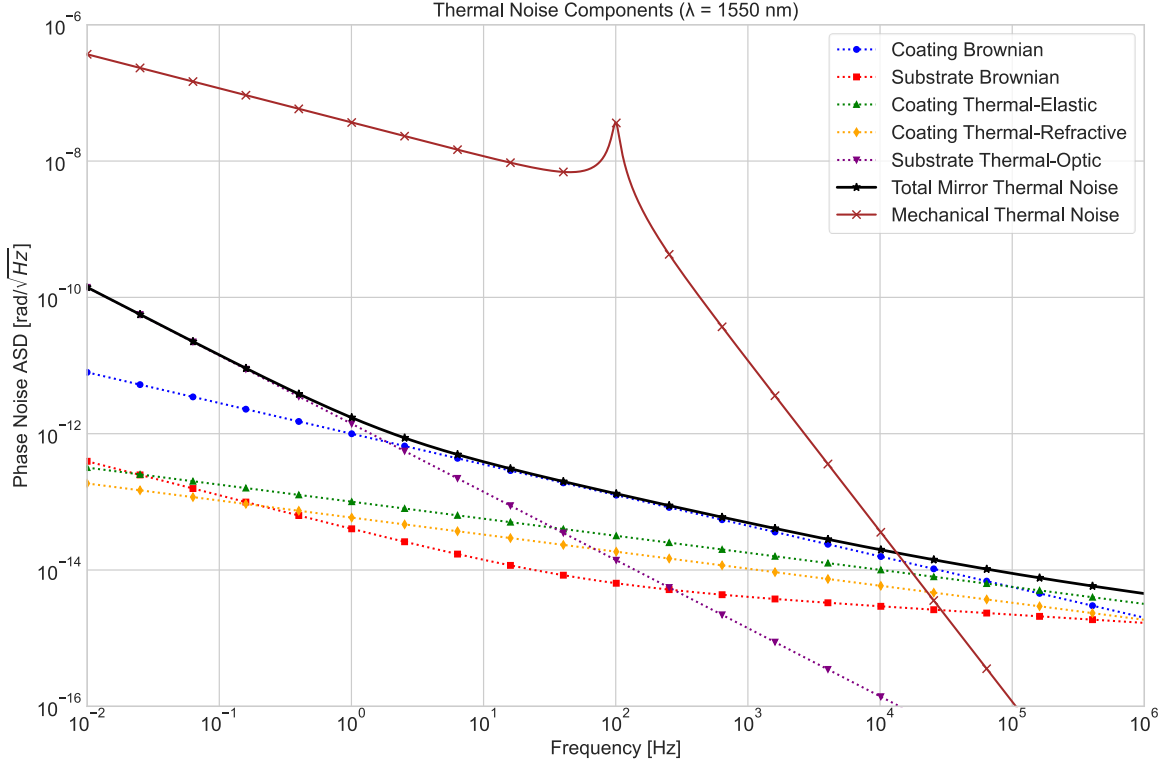


FIG. 11. Thermal noise budget order of magnitude estimate at the center carrier wavelength $\lambda = 1550$ nm.

will follow a similar treatment, but we will take into account the incoherent nature of perturbation in the VBG system. The light transmitted in the VBG system can be decomposed into parallel and orthogonal polarizations with respect to the selected axis (e.g., the crystal axis of the first input lens), described using the Jones matrix as below

$$\vec{E} = \begin{bmatrix} E_{\parallel} \\ E_{\perp} \end{bmatrix}. \quad (\text{B15})$$

Then, when the ordinary axis of the mirror/lens (including the coating) is aligned with E_{\parallel} , the transfer matrix can be represented as

$$T_{m/l} = t_0 \begin{pmatrix} 1 & 0 \\ 0 & (1-t) \exp(i\phi_{m/l}) \end{pmatrix}. \quad (\text{B16})$$

In this expression, t_0 is the overall transmission and t is the differential transmission between the two orthogonal polarization modes, which must be smaller than 100 ppm to satisfy both the loss requirement and the limits imposed by available mirror and lens coatings. In addition, $\phi_{m/l}$ is the birefringence phase shift. For a lens, it is dominated by the substrate phase shift calculated as

$$\phi_l = kd\delta n \sim 0.01 \text{ rad}, \quad (\text{B17})$$

with $\delta n \sim 10^{-7}$ for silica substrate and $d \sim 0.02$ m for the lens used in the VBG. For mirrors, the birefringent

phase shift is determined by the coating and is estimated to be $\phi_m \sim 10^{-4}$ rad for the $\text{Ta}_2\text{O}_5/\text{SiO}_2$ coating that we plan to use [158, 159]. When the optic axis of the mirror or lens is rotated by an angle $-\theta$, the transform matrix becomes

$$T_{m/l}(\theta) = T_{m/l}R(\theta), \text{ with } R(\theta) = \begin{pmatrix} \cos \theta & -\sin \theta \\ \sin \theta & \cos \theta \end{pmatrix}, \quad (\text{B18})$$

where we take the crystal axis of the last optical component as the reference frame. Suppose there is a perturbation $\delta\theta$. Then, to the first order, one obtains that

$$\begin{aligned} T_{m/l}(\theta + \delta\theta) = & t_0 \begin{pmatrix} 1 & 0 \\ 0 & e^{i\phi_{m/l}} \end{pmatrix} R(\theta) \\ & - t_0 \begin{pmatrix} 0 & 0 \\ 0 & e^{i\phi_{m/l}} \end{pmatrix} R(\theta)t \\ & - t_0 \begin{pmatrix} 1 & 0 \\ 0 & e^{i\phi_{m/l}} \end{pmatrix} R(\theta)J\delta\theta, \end{aligned} \quad (\text{B19})$$

where $J = \begin{pmatrix} 0 & 1 \\ -1 & 0 \end{pmatrix}$. The static, unperturbed transform can be corrected at the end by applying the inverse of the transform as

$$T^r = R^\dagger(\theta) \begin{pmatrix} 1 & 0 \\ 0 & e^{-i\phi_{m/l}} \end{pmatrix}. \quad (\text{B20})$$

For **non-polarization encoding**, the first-order effect is the conversion of one polarization mode into its orthog-

onal counterpart, with a conversion factor $t_0 e^{i\phi} \delta\theta$. If one polarization mode is taken as the fundamental mode, this results in a loss of $\delta\theta^2 \sim 1$ ppm given $\delta\theta_{rms} \sim 1$ mrad [45], which can be safely neglected, since the transverse mode conversion loss induced by misalignment is larger. The associated phase noise is only a second-order effect, with a factor $\sim i\phi_{m/l}\delta\theta_1\delta\theta_2$ due to the back-conversion from the orthogonal polarization mode. This yields a phase noise contribution of $\delta\phi \sim \phi_{m/l}\delta\theta_{rms}\delta\theta \sim 10^{-5}\delta\theta$, which is negligible and dominated by other rotation misalignment coupling mechanisms. An alternative interpretation is that the light in the orthogonal mode is uncorrelated with the light in the parallel mode, so the net effect is a reduction in the visibility of the fundamental mode. Provided that the power in the orthogonal mode is not significant (propagating through fewer than 10^6 sections), this effect can be safely neglected.

For **polarization encoding**, birefringence can lead to phase noise between the two encoded states $|0\rangle$ and $|1\rangle$. The difference in transmission rate, t , may also introduce amplitude noise. However, these static and known birefringence effects act as a unitary for which we can compensate. The naive solution is to alternate the orientation of the optic axis of sequential lenses between 0° and 90° , which allows for the cancelation of the transmission difference and phase shift difference between the two polarized modes. However, the sequential unknown misalignment angle $\delta\theta$ is randomized and may still introduce phase noise and amplitude noise, which is estimated here. We assume the phase difference between the two modes is ϕ_0 . Then, the input Jones matrix can be written as

$$|\psi\rangle \sim \vec{E} = \begin{bmatrix} E_{\parallel} \\ E_{\perp} e^{i\phi_0} \end{bmatrix}. \quad (\text{B21})$$

We can derive the transform matrix for two consecutive lenses/mirrors as

$$\begin{aligned} T_{1,m/l} \left(\frac{\pi}{2} + \delta\theta_2 \right) T_{2,m/l}(\delta\theta_1) &\approx t_0^2 \times \left\{ (1 - \bar{t})I \right. \\ &- \delta t_1 \begin{pmatrix} 0 & 0 \\ 0 & 1 \end{pmatrix} - \delta t_2 \begin{pmatrix} 1 & 0 \\ 0 & 0 \end{pmatrix} \\ &+ i(\delta\phi_1 - \delta\phi_2) \begin{pmatrix} 0 & 0 \\ 0 & 1 \end{pmatrix} \\ &\left. - \delta\theta_1 \begin{pmatrix} 0 & 1 \\ -1 & 0 \end{pmatrix} - \delta\theta_2 \begin{pmatrix} 0 & e^{i\bar{\phi}} \\ -e^{-i\bar{\phi}} & 0 \end{pmatrix} \right\}, \end{aligned} \quad (\text{B22})$$

where we set $t_i = \bar{t} + \delta t_i$, $\phi_{m/l,i} = \bar{\phi} + \delta\phi_i$ for each lens/mirror to separate the relatively small statistical differences of each lens/mirror. The second-order terms are not included, as it is a well-known fact that they contribute only to the trivial Kraus operators [160].

The second and third terms can be decomposed into an overall attenuation channel and a dephasing channel, respectively, while the fourth term describes dephasing due to inhomogeneous phase fluctuation, whose contribution has already been calculated in the thermal-optic noise section. The final two terms are directly associated

with misalignment effects and are expected to provide the dominant contribution: the first term corresponds a bit flip error, while the second term represents the combined effects of a bit flip and a phase shift. By averaging over these effects, one can derive a set of effective Kraus operators for each lens or mirror as follows,

$$\frac{\delta\theta}{\sqrt{2}} \left\{ \begin{pmatrix} 0 & 1 \\ -1 & 0 \end{pmatrix}, \begin{pmatrix} 0 & e^{i\bar{\phi}} \\ -e^{-i\bar{\phi}} & 0 \end{pmatrix} \right\}. \quad (\text{B23})$$

5. Acoustic Wave Noise

Acoustic noise will introduce phase noise in the VBG. Because the residual gas pressure is roughly 1 Pa, there is finite acoustic transmission from the tube walls to fluctuations in the effective refractive index of the gas in the tube. Although the ambient acoustic noise levels vary substantially in the continental US, we can adopt a representative median level for our noise budgeting purposes, assuming that the majority of the VBG will be buried ~ 2 m underground.

In UHV systems, such as LIGO, acoustic waves are heavily attenuated. In contrast, for our the mild vacuum conditions considered here, we must estimate the acoustic isolation quantitatively. The following analysis is performed with the simplifying assumption that N_2 dominates the residual gas composition.

Attenuation. In the continuum regime, the attenuation of the acoustic wave in gas is given by the classical Stokes-Kirchhoff formula [161],

$$\alpha_{SK} = \frac{\omega^2}{2\rho_0 c_s^3} \delta_{eff}, \quad (\text{B24})$$

where $\rho_0 = PRT/M$ is the gas density, with $M \approx 2.8$ g/mol being the molar mass of nitrogen, and $c_s = \sqrt{\gamma RT/M}$ is the adiabatic acoustic wave speed, with $\gamma = 1.4$ being the adiabatic index. Here,

$$\delta_{eff} = \frac{4}{3}\eta + \eta_B + (\gamma - 1)\frac{\eta}{Pr} \quad (\text{B25})$$

is the effective dissipation parameter that includes the contributions from shear viscosity ($\eta \approx 1.78 \times 10^{-5}$ Pa · s), bulk viscosity ($\eta_B \approx 0.8\eta$), and thermal conductivity, with $Pr \approx 0.72$ being the Prandtl number.

However, the continuum assumption may break down at medium vacuum for high frequency acoustic waves ($f \ll \frac{\rho_0 c_s^2}{2\pi\delta_{eff}} \sim 5$ kHz). In this region, the attenuation per wavelength ($\alpha_s \lambda_s$) saturates as predicted by the super-Burnett theory [162], and we can use the experimentally measured value for normal air as $\alpha_M \lambda_s \sim 2.5$ [163]. Moreover, to bridge the limit and the classical Stokes-Kirchhoff prediction, we use a simple and empirical saturation function as

$$\alpha_s = \frac{\alpha_{SK}}{1 + \alpha_{SK}/\alpha_M}. \quad (\text{B26})$$

Phase Shift. At low pressure, the refractive index of the residual gas scales linearly with pressure P as [164]

$$n(P) = 1 + \alpha P, \quad (\text{B27})$$

where $\alpha \approx 3 \times 10^{-9}/\text{Pa}$. Let δP denote the pressure vibration introduced by the acoustic wave, then the refractive index changes as

$$\delta n = \alpha \delta P. \quad (\text{B28})$$

Thus, the effective optical path length gain of the fundamental mode is given by

$$\delta z_{\text{eff}} \approx L_{\text{eff}} \alpha \delta P, \quad (\text{B29})$$

with L_{eff} denoting the effective length influenced. For a conservative upper bound, we assume that the coherence length is shorter than both the attenuation length l_s and the section length L_0 , such that L_{eff} is given by a Poisson process,

$$L_{\text{eff}} \sim l_c \sqrt{\frac{L_0}{l_c}} = \sqrt{L_0 l_c}, \quad l_c = \min(l_s, L_0). \quad (\text{B30})$$

The acoustic wave pressure, δP , excited by the tube oscillation (the seismic/acoustic translational input $z_t(f)$) can be calculated by

$$\delta P(f) = Z_{\text{air}} v(f) = \rho_0 2\pi c_s f z_t(f). \quad (\text{B31})$$

For a conservative estimate, it is assumed that the tube is roughly 2 meters beneath the ground, and the surrounding soil naturally acts as passive isolation, resulting in an attenuation calculated as [117]

$$\frac{z_t(f)}{z(f)} \equiv T_{\text{dirt}} = \exp\left(-\frac{\pi f}{Q_{\text{dirt}} V_s} D\right), \quad (\text{B32})$$

with $D \approx 2m$ being the depth, $Q_{\text{dirt}} \approx 10$ denoting the typical quality factor of the soil [165], and $V_s \sim 300 \text{ m/s}$ representing the typical shear wave speed, as mentioned earlier [166]. Finally, it yields a total coupling coefficient of

$$g_{aw} = \rho_0 2\pi c_s f \sqrt{L_0 l_c} \exp\left(-\frac{\pi f}{Q_{\text{dirt}} V_s} D\right). \quad (\text{B33})$$

The boundary excitation represents another coupling mechanism for the ground translational movement input $z(f)$. The coupling factor given by the boundary excitation grows linearly but is also exponentially suppressed by attenuation at high frequency, resulting in a maximum optical path length coupling factor of roughly 10^{-5} . When one compares it to the maximum suppression factor given by PIP, which is no more than 10^{-3} , we expect that this effect is dominated by the seismic and alignment noise.

Mode Loss. The acoustic wave may also introduce mode loss, which can be approximated using the Jacobi-Anger approximation as [119]

$$l_{ac} \sim 1 - J_0^2(m) = \frac{m^2}{2}, \quad (\text{B34})$$

where $m = k\delta z_{\text{eff,rms}}$ is the modulation depth. For boundary excitation, this effect is not a concern since the associated loss is dominated by the misalignment.

6. SLS Noise

The SLS system will lock the section length between neighboring mirrors (3-section) to the linewidth of the AUX laser, which helps actively suppress length fluctuations at low frequencies. However, the rough movement of the VBG itself is relatively stable at high frequencies, where the sensor noise will probably dominate and needs to be filtered out for optimized performance. The actuator noise is usually negligible compared to the sensing noise [21]. Therefore, the PSD after stabilization can be written as,

$$\hat{S}_\phi = S_{\text{SLS}} |\text{LPF}|^2 + S_\phi |\text{HPF}|^2, \quad (\text{B35})$$

where LPF and HPF are the low-pass and high-pass filter functions that satisfy the causality constraint such that $\text{LPF} + \text{HPF} = 1$. S_{SLS} denotes the total sensing noise of the SLS scheme, and S_ϕ denotes the PSD of the open-loop phase noise.

There are two dominant sources of the SLS sensing noise, namely the detection shot noise and the laser frequency noise, the former of which is given by [167],

$$S_{\text{SLS,Shot}} = \frac{hc}{\lambda \eta P_s}, \quad (\text{B36})$$

where $P_s \approx 1\mu\text{W}$ is the receiving power [168] and $\eta \approx 0.8$ is the typical detection efficiency. Estimating the frequency noise is somewhat complicated, since only two ultra-stable lasers are used for the entire system, causing the section noise to add coherently at low frequencies. For round trip detection, the average section noise is upper-bounded as

$$S_{\text{SLS,Freq}} \approx N S_\nu \frac{4 \sin^2(2\pi f \tau)}{f^2}, \quad (\text{B37})$$

where $\tau = \frac{L_0}{c}$ is the one-way delay and $S_\nu \approx (6.4 \times \frac{10^{-5}}{f} + 1.4 \times 10^{-4}) \text{ Hz}^2/\text{Hz}$ is the frequency instability of the ultra-stable laser [169]. $N \sim 10^4$ is the typical number of sections. The total SLS noise is also plotted in Fig. 9 in comparison to the LIGO ALS residual movement data [170]. The latter is roughly an order of magnitude smaller than our theoretically estimated sensing noise floor, and thus we believe the current estimate is achievable.

To obtain the precise shape of the filter functions, the usual approach is to model the entire feedback control system and optimize the transfer function to achieve the lowest residual noise. However, we can approximate it with the following simple 6th-order LPF,

$$\text{LPF} = \frac{\binom{6}{3} s^3 + \binom{6}{2} s^2 + \binom{6}{1} s + 1}{(1+s)^6}, \quad (\text{B38})$$

where $s \equiv i \frac{f}{f_c}$ with cut-off frequency $f_c \sim 5$ Hz, which can be optimized as long as $f_c \ll \frac{1}{2\tau} \sim 10^4$ Hz [171]. In terms of ASD, such a filter provides f^4 suppression of the open-loop phase noise at low frequencies and a $1/f^3$ roll-off for the sensing noise.

The post-SLS phase noises of the VBG are plotted as the red solid curve with triangle markers in Fig. 9, where the upper boundary of the red shaded area indicates the noise in the high seismic input case. Although the seismic input significantly increases in this case, the normalized residual rms noise after SLS is roughly at the level of ~ 5 mrad/km, representing a degradation of less than one order of magnitude and indicating satisfactory interference stability even in relatively noisy environments.

We remark that for applications that do not require real-time signal processing, feedback control is not necessary, and an offline post-subtracting method can be applied using the sensing data from the SLS system. This approach can result in lower noise, as the filter shape can be chosen freely without the limits of causality or stability requirements (e.g., a nearly perfect Heaviside Function).

Appendix C: Performance of Memory Configuration

It is not surprising that the VBG can be considered as a very large, high-Q optical cavity since its initial motivation, LIGO, is itself such a system. The idea of employing an optical cavity as quantum memory has long been investigated [172, 173], the principle of which is to use the techniques from building a Q-Switch cavity [47, 174] to implement the read and write operations. Employing sections of the VBG as quantum memory (VBGQM) will be particularly convenient and suitable for quantum communication protocols that require memory and are executed on the VBG. VBGQM has many advantages: a very broad bandwidth, a sufficiently long storage time, room temperature operation, and no need for conversion into matter qubits. Some particular designs for VBGQM are shown in Fig. 12.

The performance of VBGQM can also be characterized by the attenuation and dephasing of the optical quantum state after a storage time of T . The decay of the probability of successful retrieval of the quantum state can be written as

$$P_{\text{success}} = \exp(-\alpha_{\text{tot}} cT), \quad (\text{C1})$$

with α_{tot} being the attenuation factor. For the memory configuration, the beam is reflected using a steering mirror. Assuming a mechanical switch is used, the angle alignment is essential and dominates the attenuation factor, as

$$\begin{aligned} \alpha_{\text{tot}} &\approx -\frac{10}{L_0} \log_{10}(1 - 2k^2 \omega_0^2 \delta\beta^2) \\ &\sim 1 \times 10^{-4} \text{ dB/km} \sim 0.03 \text{ dB/ms}, \end{aligned} \quad (\text{C2})$$

for $\delta\beta \sim 0.05 \mu\text{rad}$ and $L_0 = 4$ km. For an EOM/PBS switch, the loss is dominated by these optical elements, which will introduce a loss at the 0.1% level [175], corresponding to an effective attenuation of 1×10^{-3} dB/km.

However, $\frac{3 \text{ dB}}{\alpha_{\text{tot}}} \sim 100$ ms is not the actual memory lifetime of VBGQM, from which one may expect the normal VBG attenuation analysis. In the VBGQM configuration, the static misalignment of the two mirrors can give rise to coherent effects since the pulse is reflected multiple times within the same section, thereby violating the stochastic accumulation assumption. In this case, it is necessary to consider coupling to the neighboring mode $(0, \pm 1)$ and to represent the beam as a vector that includes the information for both mode spaces as

$$\vec{E} = \begin{pmatrix} E_{00} \\ E_{0|\pm 1} \end{pmatrix}. \quad (\text{C3})$$

Under this representation, the truncated conversion matrix, up to the second order of the mirror M_i misalignment angle $\delta\beta$, can be derived as [120]

$$M_i = \begin{pmatrix} \sqrt{1 - \frac{1}{2}\gamma_i^2} & \frac{\sqrt{2}}{2} i \gamma_i \\ \frac{\sqrt{2}}{2} i \gamma_i & \sqrt{1 - 2\gamma_i^2} \end{pmatrix}, \quad \gamma_i \equiv k\sqrt{2}\delta\beta_i w_i, \quad (\text{C4})$$

with w_i being the spot size at the mirror's location. In addition, the propagation matrix between the two mirrors can be written as

$$L_p = \sqrt{1 - l_{\text{other}}} \begin{pmatrix} 1 & 0 \\ 0 & e^{i\phi_g} \end{pmatrix} \quad (\text{C5})$$

where ϕ_g is the Gouyo phase [176, 177] determined by the separation between the two mirrors, and l_{other} represents the additional loss that is not related to angular misalignment. Therefore, the round-trip process can be described by the following product of matrices:

$$C_{\text{cavity}} = M_1 L_p M_2 L_p^\dagger. \quad (\text{C6})$$

Assuming the configuration shown in Fig. 12(a), in which half of a standard VBG section is used for quantum memory with a plane mirror acting as the switch, the attenuation performance of the VBGQM in the presence of static angular misalignment is shown in Fig. 13 and compared with the stochastic assumption. We observe that coherent interference shortens the effective storage time by two orders of magnitude for both the common and reversed tilting cases. One may ask whether we can convert the power in $(0, \pm 1)$ mode back to the $(0, 0)$ mode to avoid this effect. Unfortunately, that option would require precise knowledge of the misalignment angle and advanced spatial mode conversion techniques, the latter of which may introduce additional losses.

In addition, we note that the cycle time of the VBGQM is limited both by the length of the VBG section and the speed of the I/O switch, i.e. $\tau_c \geq \text{Max}(\tau_{\text{switch}}, 2\frac{L_0}{c})$. In general, the round-trip time for a single VBG section will

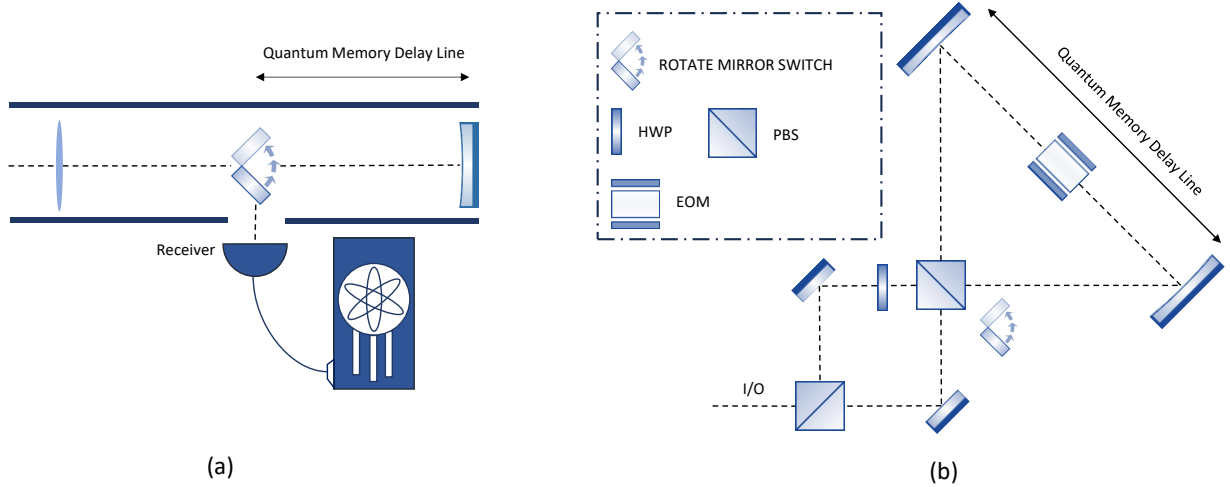


FIG. 12. A simple illustration of the design options for the VBGQM. (a) A simple design utilizes a mechanical rotating mirror to perform the I/O operation to the VBGQM. The memory delay line is a section of the VBG. (b) A more complicated design with either an electro-optic modulator (EOM) or mechanical rotating mirror to perform the I/O operation. The EOM may enable ultrafast switch time, but it may also introduce an additional 1% loss per cycle, which may seriously harm the performance of VBGQM. The memory delay line is also a section of the VBG, but with lenses on both sides replaced by mirrors.

be approximately $30\mu s$, which dominates the switch time regardless of whether an EOM switch or a mechanical switch is employed. The resulting trade-off between cycle time and total storage time has long been recognized as a serious limitation of this kind of cavity-based optical storage.

We can also estimate the number of modes for frequency division multiplexing within a VBGQM using the free spectral range $\delta\nu$ for a simple cavity as

$$\#\text{Modes}_{\text{FDM}} = \frac{\Delta\nu}{\delta\nu} = \frac{2L\Delta\lambda}{\lambda^2} = 3 \times 10^8, \quad (\text{C7})$$

which demonstrates a substantial capacity to store optical quantum signals of different frequency modes simultaneously. An alternative interpretation of Eq. (C7) is that the pulse length of the encoded bosonic information must be shorter than L to keep it completely stored in the cavity. While the ability to perform time division multiplexing is limited by the switching speed if each pulse needs to be controlled independently, the maximum number of pulses that can be stored inside the VBG cavity is given by

$$\#\text{Modes}_{\text{TDM}} = \frac{2L_0}{c\tau_{\text{switch}}}. \quad (\text{C8})$$

For a mechanical switch operating at the microsecond timescale, the storage capacity is limited to only tens of pulses. However, if all pulses are stored for the same duration, the maximum number of pulses is instead limited by the pulse width τ_p . In contrast, for an EOM/PBS switch, the switching time can be comparable to or shorter than the pulse duration [178].

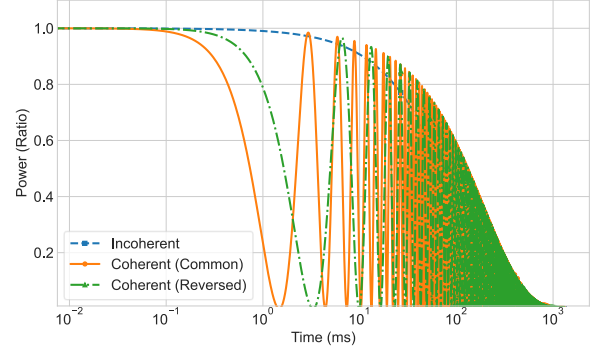


FIG. 13. Residual power ratio in the fundamental mode versus storage time of VBGQM, assuming coherent effects from common static tilting and reversed static tilting of the two mirrors by an angle $\delta\beta$, and compared with the stochastic scheme.

As for the phase noise, the situation is more subtle than in the transmission case, since the light makes repeated round trips within the same section with a round-trip time $\tau = \frac{2L}{c}$, so now the noises may add coherently instead of following a Poisson process. We adapt a similar technique to relate the phase noise PSD of the signal after N storage cycles to the phase noise PSD associated with a single round trip $S_{\phi_r} \approx 2S_{\phi_L}$, which represents the single section phase noise PSD of the VBG channel. This value can be calculated by multiplying Fig. 9 with $L = 4\text{km}$. Let $\delta\phi_r(t)$ denote the simple round trip phase noise at time t , and then the total phase noise is esti-

mated as

$$\delta\phi(N) = \sum_{n=0}^{N-1} \phi_r(n\tau). \quad (\text{C9})$$

In the frequency domain, the time delay acts as a phase shift factor $e^{-i2\pi f n\tau}$, after which one takes the sum to obtain the transfer function

$$|H(f)|^2 = \frac{\sin^2(N\pi f\tau)}{\sin^2(\pi f\tau)}, \quad (\text{C10})$$

and the PSD of the signal is related to the PSD of the single round-trip phase noise PSD as

$$S_\phi(f) = 2S_{\phi_L}(f) \frac{\sin^2(N\pi f\tau)}{\sin^2(\pi f\tau)}. \quad (\text{C11})$$

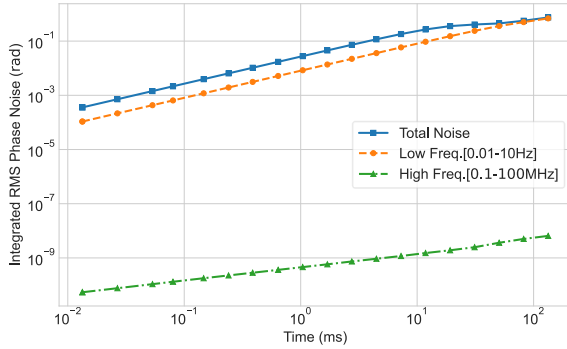


FIG. 14. RMS phase noise of the VBG integrated over the whole phase noise PSD versus storage time after active cancellation, as well as the contributions from low and high frequencies.

This relation can also be derived by viewing the VBG cavity as an F-P etalon and calculating the final phase response. When $f \ll \frac{1}{\tau}$, the pulse experiences coherent noise on each round trip. Thus, the effective transfer factor is N^2 , corresponding to a quadratic decay. In the high-frequency region, $f \gg \tau$, only the average value of this factor matters since the function oscillates quickly. Therefore, we find that

$$|H^2| \propto \frac{1}{2\pi} \int_{-\pi}^{\pi} \frac{\sin^2(Nx)}{\sin^2(x)} dx = N, \quad (\text{C12})$$

which represents linear growth characteristic of a Poisson process and can be understood as the high-frequency noise at different cycles not being correlated. Fortunately, unlike in the VBG channel case, the sensing of the error, and thus the active noise cancellation, is not limited by the round-trip delay because it is performed locally. In principle, the error can be sensed in real time and with $\tau \sim 1 \mu\text{s}$ limited by the sensing time. After cancellation, the noise is now just the sensing noise, which

is dominated by frequency noise. However, because the expected number of sections is reduced to $N \sim 100$ due to attenuation, the corresponding section noise ASD is suppressed by an order of magnitude. The RMS noise of the VBG memory channel versus storage time, obtained by integrating over the frequency range $0.01 - 10^8 \text{Hz}$, and the low and high frequency contributions, is shown in Fig. 14. The observed scaling matches our previous prediction well.

Appendix D: Enhancement of Frequency Transfer

The investigation of frequency transfer has persisted over several decades [36] due to its profound significance in the field of metrology. This endeavor has seen continual advancements in accuracy, exemplified by the implementation of extensive fiber optic linkages [133, 179–182] and, more recently, through atmospheric free-space connections [183]. A key performance metric in such systems is the additional fractional frequency instability introduced by the transmission channel. This instability is commonly quantified by measuring the interference between an ultra-stable laser and its signal after a round-trip propagation through the channel. The results are typically reported in terms of the modified Allan deviation (MDEV) or the frequency noise PSD.

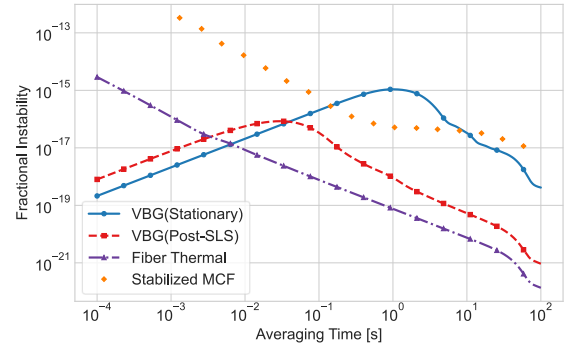


FIG. 15. Added fractional frequency instability for 25 km transmission through the VBG with and without active noise cancellation, quantified by modified Allan deviation as a function of averaging time. The results are compared with the fiber thermal noise floor [41–43] and the state-of-the-art multi-core fiber (MCF) frequency transfer experiment data [184].

The MDEV can be calculated from the PNPSD in the continuous limit via [19, 185]

$$\sigma_y^2(\tau) = \frac{2}{\nu_0^2} \int_0^\infty S_\phi(f) \frac{\sin^6(\pi f\tau)}{(\pi\tau)^4 f^2} df, \quad (\text{D1})$$

with τ as the averaging time and ν_0 as the carrier frequency. Figure 15 presents the VBG performance derived from the PNPSD, with and without SLS, alongside fiber transfer results [184]. The -1 slope in both

the VBG (SLS) and the fiber thermal floor is due to the common $1/f$ noise sources, as is typical in precision experiments [43, 186]. The $-3/2$ slope in both the stabilized MCF and fiber thermal floor indicates white phase noise. The minor hump in both VBG curves arises from the rapid roll-off of the seismic noise. Overall, the figure illustrates that the VBG achieves superior short-term stability with significantly reduced high-frequency noise compared to fiber techniques, even in the absence of SLS. Moreover, when SLS feedforward is employed, the long-term stability approaches the fiber thermal floor within an order of magnitude.

Appendix E: Performance Analysis of Additional Protocols

We summarize the key performance metrics of the VBG and the dependence of the mentioned protocols on these metrics in Table. II, supplementing Fig. 3 in the main text.

1. Quantum Position Verification

Position verification is an interesting task of significant practical importance. In many real-world scenarios, the server may want to confirm that the clients are located within the area that complies with the service contract, but the clients may not always be honest. Thus, position verification can be performed by exploiting the limitations imposed by special relativity, similar to Relativistic-QKD [58]. For simplicity, we consider only the one-dimensional case and suppose the two verifiers, separated by L , want to verify that the client is indeed located at the midpoint between them. A typical method for position verification is shown by Fig. 16, where the prover is required to compute a function whose inputs are transmitted at the speed of light from two verifiers and to return the result in a time window such that the overlap of the light cones constrains the prover's location. However, since classical information can be copied, the two attackers can easily emulate a fake position by exchanging their received inputs. It has been proven that secure classical position verification is impossible [187].

The classical limitation can be overcome by exploiting ideas from quantum key distribution, where the quantum nature of the information inherently prohibits perfect copying. Numerous research studies have been conducted on this topic [60–62], and we consider a hallmark protocol that is executed as follows [61]:

1. **Random Generation.** The Verifiers, V_0 and V_1 , choose two strings of random bits, v_0 and v_1 , of length n . Let f be the inner product function.
2. **Quantum State Transmission.** If $f(v_0, v_1) = 0$, V_0 prepares a qubit Q in the Z basis. Otherwise, Q is prepared in the X basis.

3. **Classical Bit Transmission.** V_0 and V_1 send v_0 and v_1 to the Prover P and engineer the timing so that Q, v_0 , and v_1 reach the position they want to verify, z , at the same time.
4. **Measurement.** If $f(v_0, v_1) = 0$, the prover measures Q in the Z basis. Otherwise, it is measured in the X basis.
5. **Certification.** The Prover sends back the measurement results b to the two verifiers immediately after receiving Q at the speed of light.
6. **Verification.** The verifiers check whether the measurement result is correct and whether the measurement result arrived in time. The above procedure is repeated for r rounds to achieve the desired confidence.

In contrast to the QKD case, verifiers in QPV cannot trust any party; consequently, attackers may also exploit entanglement to compromise the protocol. It has been shown that such attacks are always possible if two adversaries share an exponential number of entangled qubits [188]. However, the above protocol is proven to be secure if attackers control fewer than $o(n)$ qubits under reasonable computational time constraints [189].

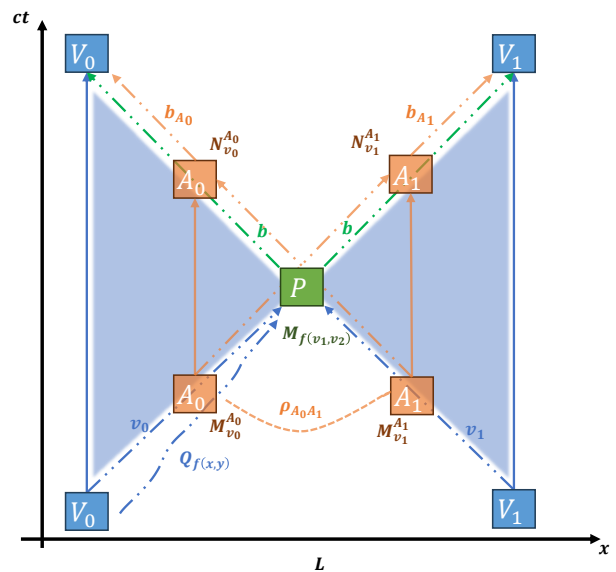


FIG. 16. Illustration of the typical QPV protocol. The shaded regions represent the future light cones of both verifiers, with P being the only intersection point in the ideal case. The orange boxes indicate the two possible attackers attempting to spoof the location using a pre-shared resource state with one-round simultaneous communication.

The implementation of large-scale QPV protocols is mainly limited by the attenuation in the single qubit

TABLE II. Summary of VBG's Performance Metrics and Applications Requirements*

Metrics	Attenuation (dB/km)	Linewidth (THz)	Phase (rad/ $\sqrt{\text{km}}$)	Polar. (Prob/km)	Trans. Speed (c)	Pulse Dur. (fs)
VBG Data	$\sim 4 \times 10^{-5}$	~ 6	$\sim 10^{-3}$	~ 1 ppm	$\sim 1 - 10^{-5}$	≥ 50
Secure Quantum Communication						
DI-QKD [49–57] (Sec. III A)	✓	✓	–	○	–	–
QPV [60–62] (Appendix E 1)	✓	✓	–	○	✓	–
R-QKD [31, 58] (Appendix E 2)	✓	✓	✓	–	✓	–
QPQ [59] (Appendix E 2)	✓	✓	–	–	–	–
MPED [63–67] (Appendix. E 2)	✓	✓	–	–	–	–
Distributed Quantum Sensing						
QTelescope [68–70] (Sec. III B)	✓	○	✓	–	–	–
QCN [71–73] (Appendix E 3)	✓	✓	✓	–	–	✓
GOG [74–76] (Appendix E 4)	✓	✓	✓	–	–	✓
Federated Quantum Computation						
QDC [77, 78] (Appendix E 5)	✓	✓	–	–	✓	–
BQC [79, 80] (Sec. III C)	✓	✓	–	–	○	–
NLQC [81–83] (Appendix E 6)	✓	✓	–	–	–	–

* '✓' means the specific application relies on a certain performance metric, while '–' infers that it is less relevant, and '○' suggests that it may depend on a concrete protocol.

transmission in each round, which introduces a non-zero failure probability estimated as $0.5\bar{\alpha}$ for the honest prover, with $\bar{\alpha}$ being the average attenuation. In addition, the attackers still have a non-zero probability of success, $1 - p_a$, even under the assumption of limited quantum resources, and thus set a threshold for the attenuation. Suppose we require the honest prover to succeed and the attackers to fail with the same confidence level (CL), the expected rounds r can be calculated using Hoeffding's inequality as

$$r \geq -\frac{2 \ln(1 - \text{CL})}{(p_a - 0.5(1 - \eta))^2}, \quad 1 - \eta \geq 2p_a. \quad (\text{E1})$$

Dividing by the multiplexing factor $\Delta\nu$ gives the minimum execution time, $\tau_{\text{ex}} \approx \frac{r}{\Delta\nu}$. For the inner product function, we chose $p_a \approx 0.1$; however, we note that although more advanced protocols have been developed to avoid this threshold, they require additional quantum operations, such as quantum non-demolition detection [62].

The minimum execution time, τ_{ex} , versus the distance between the verifier and the honest prover, assuming the use of the VBG for transmission, is shown in Fig. 17. It can be concluded that when the transmission distance is relatively short, the minimum execution time is at the picosecond scale, which is primarily constrained by the protocol dependent p_a and by the practically available multiplexing factor. In this regime, the execution time will be dominated by the transmission time, as the total

time consumption for the protocol is given by

$$T_{\text{tot}} = \tau_{\text{ex}} + \frac{L}{\bar{v}_g}, \quad (\text{E2})$$

where $\bar{v}_g \approx c$ is the transmission speed of the qubit through the vacuum beam guide. Furthermore, we observe that the threshold transmission distance exceeds 10^4 km if the QPV is executed via the VBG. This result demonstrates that the VBG channel effectively minimizes the impact of quantum transmission losses, such that protocol execution over continental scales will ultimately be limited by the Earth's curvature and the transmission speed of the classical bit strings rather than the quantum channel itself.

Conversely, the VBG could potentially facilitate attacks on the QPV protocol. Although existing attack methods require an exponential number of entangled qubits, the known lower bound on qubits needed for attackers increases linearly with the classical bit strings sent. Moreover, without quantum memory, attackers must transmit qubits nearly at light speed, which the VBG is capable of supporting, as demonstrated in Eq. (8) in the main text.

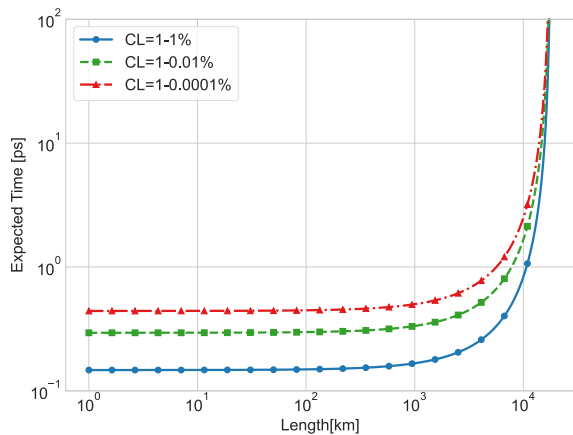


FIG. 17. Minimum execution time versus the distance between the verifiers and the honest prover under different confidence requirements.

2. General Quantum Cryptography

The two previously discussed tasks exhibit a hard attenuation threshold in the absence of advanced quantum control techniques, highlighting the irreplaceable role of the VBG in implementing these protocols in the near term. Beyond these tasks, the VBG enables fast quantum information exchange on a global scale, providing universal advantages for general quantum cryptographic protocols involving geographically isolated parties. Although these loss-tolerant protocols may be executed without the VBG over long distances, the VBG can nevertheless provide speedups of several orders of magnitude compared to existing quantum channel techniques. We will now discuss several additional qualitative examples.

Relativistic-QKD (R-QKD) [31, 58] has emerged as a focus within the QKD field due to its ability to maintain a nonzero key rate under significant channel loss and to ensure security with minimal device assumptions through special relativity constraints. The optimal performance requires qubit trajectories to align as closely as possible with a null geodesic; otherwise, a quantum memory is necessary, and the channel must exhibit strong phase reliability. The quantum signal in the VBG travels nearly at the speed of light in a vacuum, in contrast to approximately $\frac{2}{3}c$ in optical fiber. The VBG can also traverse with an effective refractive index $n_{\text{eff}} \approx 1.26$, assuming a steering mirror must be installed at a maximum of every 3 sections, in contrast to about 1.4 in satellite-to-ground links due to geographic constraints. These capabilities of the VBG significantly benefit R-QKD implementation. Additionally, the VBG phase noise after the SLS is at a level of 10^{-4} rad/ $\sqrt{\text{km}}$, and VBG-based quantum memory (VBGQM) offers millisecond-level storage without qubit conversion, as detailed in Sec. C, thereby mitigating effective refractive index deviations and enhancing

system flexibility.

Following the paradigm of QKD, the quantum private query (QPQ) protocol can be implemented using lure requests on a quantum server with quantum random access memory [59]. The randomly inserted lure request addresses, encoded in an alternative basis, enable the user to detect eavesdropping by the server with high probability. The VBG can be employed to transmit both the query and the requested data with high fidelity, which reduces the possibility of the server concealing its malicious behavior as channel loss.

Finally, multiparty entangled state distribution (MESD) over large-scale networks is being actively explored due to its potential cryptographic advantages over pairwise Bell-pair distribution [190]. In particular, quantum secret-sharing protocols [191, 192] can be uniformly described by the construction and manipulation of graph states across a network, which form a representative class of multiparty entangled states [193, 194]. Advanced and efficient network layer protocols [63–67] have been proposed for the general distribution of arbitrary graph states, in which channel capacity and reliability play crucial roles in resource allocation and optimization. If future networks are built on the backbone of the VBG channel, then the network topology is approximately star-shaped, enabling the distribution of arbitrary graph states within a single time slot, significantly reducing distribution latency and the burden on quantum memory.

3. Synchronized Network of Clocks

As depicted in Fig. 18, constructing a highly precise synchronized quantum clock network (QCN) involves two key phases: aligning local clocks to a common ultra-stable frequency standard [72] and achieving precise clock positioning and synchronization through the Einstein synchronization method [195]. Research shows that quantum protocols can enhance both of the aforementioned processes, providing a precision improvement that follows a square root scaling relative to classical techniques [71, 73]. In this framework, the deployment of the VBG can provide substantial benefits in protecting the fragile quantum signal and serves as a foundation for constructing a quantum probe of gravity [196].

Establishing a remote frequency standard is critical for real-time sensing and many other experiments involving general relativity effects [197, 198]. Quantum entanglement can be utilized to construct a global frequency standard that leverages resources from all participating nodes, with optimal scaling for short-time Allan deviation as [72]

$$\sigma_y(\tau) \sim \frac{\sqrt{\log(N)}}{\omega_0 N} \frac{1}{\tau}, \quad (\text{E3})$$

where N is the total number of qubits involved in the GHZ state, $|\text{GHZ}\rangle_N$, and ω_0 is the frequency reference of the atomic clock. An intuitive explanation is that

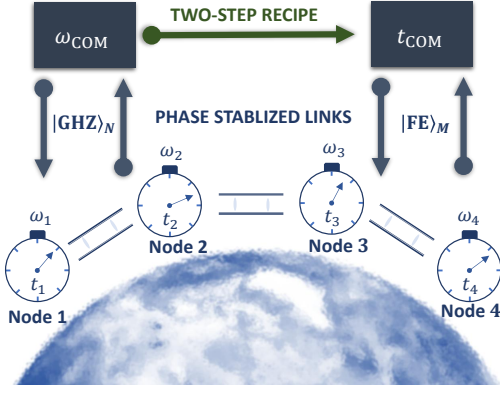


FIG. 18. Illustration of the quantum enhanced network of synchronized clocks, which involves two key steps that benefit from different types of entangled state.

these established entanglements effectively bring the distributed local resources of each node together at the logical level and allow for the collective operations required for coherent quantum enhancement. This protocol requires a multiqubit GHZ state of extremely high fidelity (~ 0.99), and thus highly transparent channels, such as the VBG, as any loss of photons destroys the GHZ state. In addition, establishing such a quantum clock network also requires robust frequency transfer between nodes to synthesize the global standard oscillator signal and implement feedback control. This task is purely classical and well-studied [36], though the VBG may also provide potential enhancement due to its lower intrinsic phase noise compared to fiber when above 1Hz, which was discussed in more detail in Sec. D.

Once the frequency of each node is locked to a common standard, the nodes can perform Einstein's protocol to eliminate the offsets of each clock. For simplicity, we assume a case involving two nodes, Alice and Bob, separated by a distance L while remaining in the same global inertial frame. The synchronization procedure works as follows:

1. Alice sends a pulse to Bob at t_a^s , as recorded by Alice's clock.
2. Upon receiving that pulse, Bob records the time t_b and reflects the pulse (or sends another pulse immediately).
3. Alice receives the reflective pulse and records the time as t_a^e .
4. The measured offset is determined as

$$\Delta t_{ab} = \left| \frac{1}{2}(t_a^s - t_a^e) - t_b \right|.$$

The above procedure is repeated and executed in M parallel modes to achieve the desired precision.

The synchronization precision relies on the measurement accuracy of t_b and t_a^e . To streamline performance

evaluation, we focus solely on the one-way transfer from Alice to Bob, assessing the variance of t_b as a positioning method, with an analogous analysis applicable for synchronization.

Using entanglement across M parallel modes can enhance measurement precision by \sqrt{M} . The frequency entangled (FE) state is assumed to be in the following form [71, 73],

$$|\text{FE}\rangle_M = \int d\omega \phi(\omega) \otimes_{i=1}^M |1_\omega\rangle_i, \quad (\text{E4})$$

where $|1_\omega\rangle_i$ is the single photon state at frequency $\Omega_i + \omega$ and $\phi(\omega)$ is the spectral function shared by M modes, with ω defined as the detuning with respect to the carrier frequency Ω_i . Then, the variance of the measurement is given by

$$\Delta t_{\text{en}}^2 = \frac{\Delta \tau^2}{M^2}, \quad (\text{E5})$$

where τ^2 is the variance determined by the envelope function,

$$g(t) = \frac{1}{\sqrt{2\pi}} \int d\omega \phi(\omega) e^{-i\omega t}. \quad (\text{E6})$$

However, attenuation in the transmission channel can seriously impact the performance of the entangled state. Suppose that any one of the photons from the M modes is lost. In that case, the state will be projected onto a diagonal density matrix in the $|\omega\rangle$ basis, which is essentially a continuous wave instead of a pulse, and thus destroys any information regarding the arrival time [73]. When the protocol is repeated for rounds $r \gg 1$, the asymptotic variance for the arrival time of each round can be calculated as

$$\Delta t_{\text{en}}^2 \simeq \frac{\tau^2}{\eta^M M^2}, \quad (\text{E7})$$

where η represents the coupling efficiency, as before. In the classical case, the information associated with any mode whose photon is not lost is unaffected, giving

$$\Delta t_{\text{cl}}^2 \simeq \frac{\tau^2}{\eta M}. \quad (\text{E8})$$

The different scaling with η gives rise to a threshold value of the coupling efficiency, below which the classical scheme is more advantageous. In addition, the channel introduces phase noise σ_ϕ^2 , as before, and the broadening of the envelope due to GVD is estimated in Sec. IID in the main text. These two effects can be shown to be identical for both the classical and entangled cases by transforming the field operators in the Heisenberg picture: the phase noise contributes an additional time variance of $\frac{\lambda^2 \sigma_\phi^2}{4\pi^2 v_g^2}$, and the GVD broadens the envelope variance according to Eq. (11) in the main text.

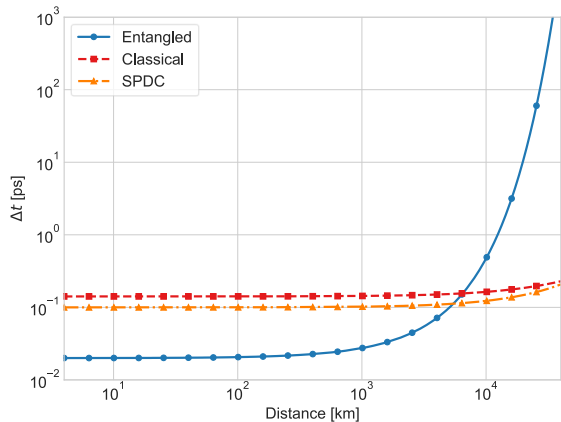


FIG. 19. Variance of the arrival time versus various separation lengths under classical, M -entangled state, and SPDC ($M = 2$) schemes. For the SPDC state, it is a partially entangled state separated into $M/2$ tensor components, with each component containing two entangled photons.

For performance estimation, we set $\tau = 1$ ps with $g(t)$ taken to be a Gaussian envelope function. The phase noise is calculated using the PNPSD as before, and the mode numbers are determined by the linewidth of the VBG, assuming frequency multiplexing as $M \approx \frac{\Delta\nu}{4\pi\tau} \approx 50$. The synchronization precision achieved using the VBG at different separation distances L is shown in Fig. 19. The quantum scheme provides approximately an order of magnitude improvement over the classical scheme over a distance range of 10^3 km, while the performance degrades significantly across 10^4 km due to coherent loss. In addition, the SPDC scheme with pairwise entanglement demonstrates a longer threshold distance but achieves only a $\sqrt{2}$ enhancement.

4. Giant Optical Gyroscope

The VBG itself is a large-scale optical platform, and it is therefore well suited for measurements that benefit from scaling up, such as the realization of a giant optical gyroscope (GOG). A quantum optical gyroscope has recently been proposed for applications in seismology and for probing the interplay between quantum physics and general relativity [74]. In this scheme, an indistinguishable photon pair is emitted into a large ring cavity attached to the Earth's surface, with one photon propagating clockwise and the other counterclockwise. The Earth's rotation, the speed of which is denoted as ω_E , induces a Sagnac effect [199] that introduces a relative time delay $\delta\tau_{\text{sag}}$ between the two photons that is proportional to the area size of the ring cavity, which can be written as

$$\tau = \mathcal{F}A, \quad (\text{E9})$$

with \mathcal{F} being the sensitive factor and A being the area size. This delay τ shifts the HOM dip, from which the time delay can be determined. In addition, general relativity predicts a correction to the locally observed angular rotation rate, known as the frame-dragging effect [200],

$$\Delta\omega_{\text{FD}} = \frac{2GI}{c^3 R_E^3} \omega_E \sim 10^{-9} \omega_E, \quad (\text{E10})$$

where G is the gravitational constant, I is the moment of inertia, and R_E is the Earth's radius. This corresponds to a sensitivity factor of $\mathcal{F}_{\text{FD}} \sim 10^{-24}$ s/km², implying that an area of 10^6 km² can only generate a time delay at the attosecond level, which lies barely within the demonstrated sensitivity of the HOM-dip measurements [201].

Such a measurement necessarily requires ultra-transparent transmission channels to preserve the photons during propagation, a regime in which the VBG offers a natural solution. At the same time, this measurement also requires a relative precision on the order of 10^{-9} , since it can be shown that the frame-dragging correction cannot be separated from the ordinary angular rotation as long as the gyroscope is located on the Earth's surface. Although the gyroscope itself benefits from common-mode noise rejection, this still imposes stringent requirements for delay line scanning, requiring micrometer-level accuracy over a cavity of thousand-kilometer scale. Furthermore, additional suppression of pulse broadening due to the lens-induced GVD is required to reduce the width of the HOM-dip.

An alternative solution is the use of the active gyroscope technique, namely the intra-cavity phase interferometer (IPI) [202, 203], which measures the resonant frequency shift rather than the time delay itself, although it operates as a classical measurement technique. Despite significant efforts toward constructing the first ground-based gyroscope capable of measuring the frame-dragging effect, current implementations remain two to three orders of magnitude away from the required precision [75, 76]. Beyond continuous wave measurement, the use of correlated frequency combs may further scale the system and eliminate the dead band arising due to cross-scattering, since the gain medium need not fill the entire cavity [204]. The precision of the measurement can also be improved using squeezed light [205], further expanding the potential of VBG channels.

5. Long-Distance Distributed Fault-Tolerant Quantum Computing

VBG technologies facilitate the development of long-range, distributed, fault-resistant quantum computing through the realization of quantum data centers (QDC), which minimally include a QRAM and quantum network interface, as illustrated in Fig. 20. The extremely low attenuation rate of the VBG is vital for preserving coherence and reducing information loss across lengthy

quantum channels [77, 108, 109]. In such architectures, the VBG can enable high quality distribution of T -gates, support remote fault-tolerant quantum computing, and allow remote distillation of magic states through high-fidelity entangling gates over long distances. These capabilities are essential for scalable quantum architectures based on modular and distributed subsystems. Such configurations have been shown to offer significant advantages in terms of data-size scaling and the efficiency of outsourcing computational tasks when fast quantum memory is available [77, 206]. For example, high-fidelity quantum teleportation not only reduces failure rates and improves Bell pair quality by suppressing attenuation but also enhances the robustness of quantum information transfer across distant nodes. This improvement directly impacts the *delay time* in distributed quantum computing architectures [77, 78], where the delay of quantum communication plays a key role in determining the performance and architecture of surface code magic state distillation schemes.

Reduced communication latency and higher gate fidelities enabled by the VBG will lead to shorter delay times and more cost-effective magic state distillation protocols. For a transmission distance d , the decay of the photonic intensity ratio will be $10^{-d\alpha_{\text{att}}/10}$. In the absence of photonic loss, the delay time will be d/c . In the presence of photonic loss, however, the delay time will be amplified by $\frac{d}{c} \times 10^{d\alpha_{\text{att}}/10}$. Thus, the relative delay time comparing the VBG with optical fiber is approximately $10^{-d\alpha_{\text{att, fiber}}/10}$ for $\alpha_{\text{att, fiber}} \gg \alpha_{\text{att, VBG}}$. The advantage, therefore, increases exponentially with distance. For instance, for $d \approx 500$ km, we have a 31% reduction in delay time. Such savings, according to Figure 3 of [78], will switch the optimal magic state distillation protocol and yield qubit savings of around 20%. Consequently, these improvements will enhance the overall throughput and scalability of distributed quantum computing and significantly improve the efficiency and reliability of quantum task outsourcing.

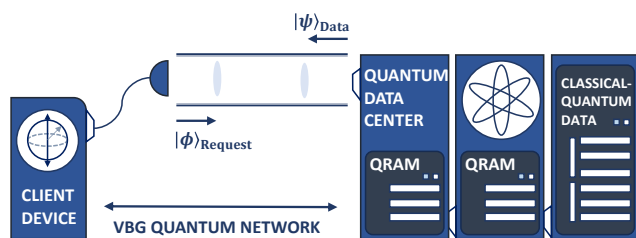


FIG. 20. Illustration of the interaction between a quantum data center (QDC) and a client’s processor via a VBG-based quantum network.

6. Non-Local Computation Tasks

Robust entanglement establishment is also essential for enabling non-local computation tasks, in which quantum mechanics offers a fundamental advantage in reducing communication costs. In the QPV section, it was mentioned that hackers may possess an exponential amount of quantum entanglement [188], which can be modeled as a non-local computation task executed with one round of communication.

The general framework of non-local quantum computation (NLQC) was first proposed and pioneered by Yao *et al.* to investigate communication complexity in a quantum regime [81–83]. In this setting, Alice and Bob receive local inputs x and y (classical or quantum) and are required to compute a function $f(x, y)$ by producing outputs a and b such that $f(x, y) = a \oplus b$. In the ideal case where the parties share a non-local box that is capable of computing $f(x, y) = x \wedge y$ nearly perfectly (with a probability higher than 90.8%), it is shown that every function can be distributively computed with just one bit of information exchange [207, 208]. This threshold is closely related to the CHSH game, in which a quantum strategy is capable of achieving an optimal success probability of approximately 85% [209]. Although this probability is insufficient to trivialize communication complexity, it still demonstrates the advantages of nonlocal quantum computation.

Beyond its role in attacks on QPV, non-local computation has concrete applications in coordinated decision-making through quantum telepathy, which can be exploited to establish an efficient stock market strategy beyond the classical limit [210]. However, if the entangled pair is distributed via a direct photonic connection, the coupling efficiency η will seriously affect the performance of the protocol and establish a threshold below which the quantum strategy cannot develop any advantages. In the simplest case in which each party receives a single input bit, the achievable distance in standard optical fiber is limited to only 10 kilometers, rendering the protocol impractical for latency-sensitive applications. However, if the VBG is used for distribution, the distance can be scaled to more than 30000 km, allowing HKEX and NYSE traders to carry out a quantum-enhanced coordinated trading strategy with a genuine operational advantage.

Appendix F: Limitations and Future Work

The results presented in this work are primarily based on first-principles analysis. While as much real measurement data is incorporated as possible and assumptions are adapted conservatively, these results are still subject to limitations, which we discuss in this section.

Construction Route. One of the major challenges in deploying such a large scale quantum infrastructure (10^4 km) is finding a suitable place to construct it. Re-

ardless of the civil and legal issues, to maintain the advanced phase stability of the VBG, it must be located and routed across a relatively quiet rural area when possible, rather than in noisy urban centers. However, this may not always be possible, and it might be inevitable to have sections going across areas with active geological or human activities (e.g., rail lines). In that case, the on-site seismic and acoustic input measurement must be performed to assess real translational and rotational motion input, so that the engineers can decide whether to make a detour or to deploy a more expensive seismic isolation platform based on budget concerns. In addition, as mentioned in Sec. A 2, we will need steering mirrors to deflect the direction of the channel to avoid man-made structures. We believe the current assumption of placing one mirror every three sections is conservative, and we anticipate geographic tomography being performed prior to the construction for an optimized route plan, similar to the approach utilized by the 40-km LIGO project [211, 212].

Ultra-low Frequency Drift. In this work, the noise spectrum under consideration extends down to $f_l \sim 0.01$ Hz, which corresponds to an observation time of 100 s that is assumed to be sufficient for most applications. As we can see from Fig. 2(b) in the main text, the RMS noise appears to saturate when the lower cut-off frequency is below 1 Hz. The lower frequency noise is dominated by low-frequency drifts due to geophysical and geodetic movement [213, 214], as well as flicker noise in the SLS sensing devices. The integrated contributions of these nonstationary noise sources diverge as $\sim \ln(1/f_l)$ with f_l approaching zero [215]. To remove these near-DC noises, either calibration against a reference or differential measurement schemes that reject the common-mode noise [216] are required. Since the performance PSD is evaluated down to 0.01Hz in this work, such mitigation procedures are expected to be conducted on a timescale around 100 s, which is feasible given that the maximum signal delay allowed in the VBG is no more than 1 s. These processes can be integrated into the ACS system, which operates on the same timescale and already partially suppresses these effects. Further decreasing the lower cutoff frequency is also possible and will not significantly change the rms noise due to the typical logarithmic scaling. The detailed analysis and budgets for these ultra-low frequency noises are beyond the scope of this work, and we look forward to future investigations for the confirmation of our cut-off frequency assumption.

Residual Gas Evacuation. In the analysis of the vacuum tube, a dry residual air condition is assumed, with the volume fractions of the constituent gases to be approximately,

$$\begin{aligned} N_2 : O_2 : Ar : H_2O : CO_2 : He : H_2 \\ \approx 0.78 : 0.21 : 0.009 : 0.001 : 0.0004 : 10^{-5} : 10^{-6}. \end{aligned} \quad (F1)$$

Importantly, water molecules exhibit several strong absorption lines in the telecom band. Therefore, maintaining a dry air condition is crucial for the fundamental performance of the VBG. In LIGO, water molecules

form strong hydrogen bonds with the metal oxide layers on the inner surfaces of the stainless steel tubes and thus require substantial effort to remove beyond simple pumping [217]. The solution adopted by LIGO involves baking the vacuum tubes for weeks prior to operation (a one-time procedure) and maintaining cryopumping with liquid nitrogen. However, for our 1 Pascal medium vacuum requirement with a 0.1% water volume ratio, the desired conditions are expected to be readily achievable using inexpensive dynamic purge techniques with dry nitrogen backfill. The residual gas pressure may be further reduced by an order of magnitude whenever such an upgrade is economical. Another concern is that light gasses, like hydrogen, are the hardest for mechanical pumps to compress and evacuate, and the stainless steel walls are constantly releasing hydrogen. While the atmospheric concentration of H_2 is only 0.5 ppm, the major residual gas component in the ultra-high vacuum environment of LIGO is hydrogen (99%) due to the bulk diffusion mechanism [218]. Since the compression ratio (K_0) for hydrogen in a lobe pump is roughly 15–20% smaller than that for air [219], we adopt a conservative hydrogen volume fraction of 1 ppm. At a total pressure of 1 Pa, the contribution from bulk diffusion is expected to remain negligible. Nevertheless, a comprehensive study of the residual gas will be required in future work to confirm the assumed mixture and its impact on system performance.

Coating Design. The reflection and absorption losses in the AR coating are based on the simulation with optimized 8-layer Ta_2O_5/SiO_2 stacks designed for the telecom band. With the introduction of the steering mirror, we assume the HR coating has a similar performance to the AR one. This assumption is conservative, given that the HR coating transmission loss is less than 5 ppm in LIGO [220], and the dominant contribution to the current steering mirror losses is from angular misalignment rather than coating absorption. For polarization encoding, the crucial point is to ensure that the HR coating maintains its attenuation performance for both polarization modes at the designed incident angle (e.g. 45°), as mentioned in Sec. B 4. Although achieving such a loss requirement for both polarizations is not difficult and has been readily demonstrated with Ta_2O_5/SiO_2 layers [221, 222], this constraint will complicate the coating design, increase thermal noise, and inflate budgets. In addition, the birefringence phase shift will also need to be compensated by carefully arranging the optic axes of the lenses. For these reasons, time-bin encoding may provide a simpler and more robust alternative. Furthermore, the assumption we made about the material properties for HR/AR coatings when estimating the Brownian noise and thermal-optics noise in Sec. B 3 may not be true if the material properties change significantly during manufacturing, especially after the doping and annealing process [223]. Therefore, a dedicated experimental characterization of coating losses and noise will be required in future work to validate these assumptions.

Control System Robustness. Although a prototype design of the control system is provided, its performance is analyzed only theoretically with reasonable redundancy, incorporating all noise sources of which we are aware. As a result, this assessment should only be taken as an order-of-magnitude demonstration until experimental measurements are performed to confirm the models. The proposed design primarily serves as a proof-of-principle guideline that can be further modified and improved through careful engineering if the model assumptions fail, designs lack a robust duty cycle, or restrictions become unnecessarily limiting. Alternative designs are also suggested at the end of the corresponding subsections. In addition to the rotational RMS noise and the ultra-low drifting issues mentioned earlier, it is noted that the AUX beam jitter [123] can raise concerns if it is too intense and rapid, drowning out the actual motion signal of the mirrors or lenses, which could cause failure in the ACS system. Encouragingly, reinforcement learning can be integrated into the control system to enhance performance and avoid overshooting due to a suboptimal control strategy [224].

Protocols Performance. The performance of the applications estimated in this work is mainly based on the limitations induced by the optical metrics imposed by the VBG channel, while neglecting other external factors such as the quality of quantum sources, photon detector efficiency, and quantum control ability. Although this approach directly probes the scalability of the protocols and unravels the intrinsic improvements and advantages of the VBG channel, it does not represent the performance that is immediately realizable in current experiments. In practice, these *one-time* losses and noise sources may constitute the dominant constraints on feasibility, particularly in regimes where the VBG channel considerably reduces the quantum communication cost. Nevertheless, we believe that the VBG is an indispensable building block for the protocols mentioned in Table. II, and the analysis presented here reflects the asymptotic performance of these protocols in the near future.

A more detailed analysis of these issues is beyond the scope of this work. However, we look forward to future investigations, especially full simulations and small-scale experimental demonstrations.